

# GenZ-LIO: Generalizable LiDAR-Inertial Odometry Beyond Indoor–Outdoor Boundaries

Daehan Lee<sup>1</sup>, Hyungtae Lim<sup>2</sup>, *Member, IEEE*, Seongjun Kim<sup>1</sup>, Soonbin Rho<sup>1</sup>, Changhyeon Lee<sup>1</sup>, Sanghyun Park<sup>1</sup>, Junwoo Hong<sup>1</sup>, Eunseon Choi<sup>1</sup>, Hyunyoung Jo<sup>1</sup>, and Soohye Han<sup>1†</sup>, *Senior Member, IEEE*

**Abstract**—Light detection and ranging (LiDAR)-inertial odometry (LIO) enables accurate localization and mapping for autonomous navigation in various scenes. However, its performance remains sensitive to variations in spatial scale, which refers to the spatial extent of the scene reflected in the distribution of point ranges in a LiDAR scan. Transitions between confined indoor and expansive outdoor spaces induce substantial variations in point density, which may reduce robustness and computational efficiency. To address this issue, we propose *GenZ-LIO*, a LIO framework generalizable across both indoor and outdoor environments. *GenZ-LIO* comprises three key components. First, inspired by the principle of the proportional–integral–derivative (PID) controller, it adaptively regulates the voxel size for downsampling via feedback control, driving the voxelized point count toward a scale-informed setpoint while enabling stable and efficient processing across varying scene scales. Second, we formulate a hybrid-metric state update that jointly leverages point-to-plane and point-to-point residuals to mitigate LiDAR degeneracy arising from directionally insufficient geometric constraints. Third, to alleviate the computational burden introduced by point-to-point matching, we introduce a voxel-pruned correspondence search strategy that discards non-promising voxel candidates and reduces unnecessary computations. Experimental results demonstrate that *GenZ-LIO* achieves robust odometry estimation and improved computational efficiency across confined indoor, open outdoor, and transitional environments. Our code will be made publicly available upon publication.

**Index Terms**—LiDAR-Inertial Odometry (LIO), Localization, Mapping

## I. INTRODUCTION

Light detection and ranging (LiDAR) sensors capture precise range measurements through laser-ray-based active sensing, while inertial measurement unit (IMU) sensors provide high-frequency inertial measurements of linear acceleration and angular velocity [1]. By fusing these complementary sensing modalities, LiDAR-inertial odometry (LIO) enables precise localization and mapping, and has been actively developed over the past decade for autonomous navigation across diverse environments [2].

Despite this active progress, LIO performance has been observed to degrade in response to two key geometric characteristics of the surrounding environment: (i) the *spatial*

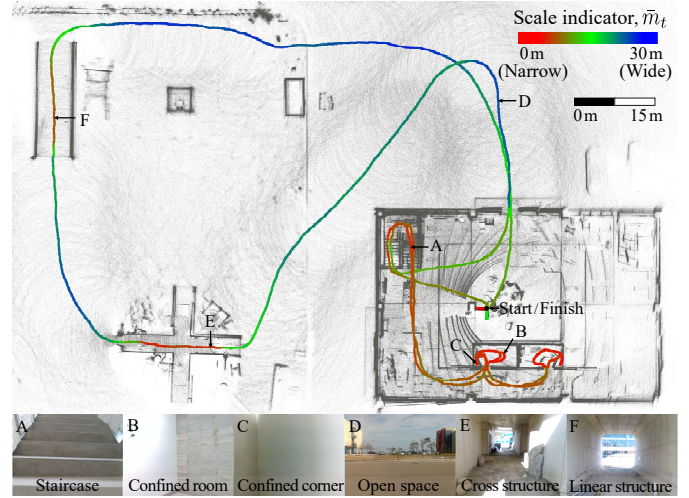


Fig. 1. Estimated trajectory and mapping result of our *GenZ-LIO* on the Handheld-A-01 sequence of our NarrowWide dataset, introduced in this work, where the platform traverses environments with substantially different spatial scales. The trajectory is color-coded by the proposed scale indicator  $\bar{m}_t$ , which reflects the spatial extent of the surrounding scene. By incorporating this indicator, *GenZ-LIO* adapts to varying scene scales, enabling consistent odometry estimation while maintaining computational efficiency across both confined indoor and open outdoor environments.

*scale* of the scene, and (ii) the *local geometric structure* that governs the reliability of different error metrics. Regarding spatial scale, which refers to the spatial extent reflected in the distribution of point ranges within a LiDAR scan, any mismatch between a fixed voxel size and the actual scene scale can disrupt both pose estimation stability and computational efficiency [3]–[5]. This issue is closely related to the use of a fixed voxel downsampling resolution (i.e., voxel size) that is typically pre-tuned for a specific expected scene scale. For instance, a large voxel size pre-tuned for outdoor scenes becomes excessively coarse when the robot enters narrow indoor spaces, oversimplifying geometric structure and degrading estimation accuracy [4], [5]. Conversely, a small voxel size pre-tuned for indoor scenes becomes overly fine in wide outdoor environments, resulting in an excessively large number of voxelized points and increased computational load [3].

Regarding local geometric structure, the appropriate error metric for scan-to-map alignment depends on whether the environment supports planar modeling [6]. In confined indoor scenes, LiDAR points tend to be densely distributed and often form locally planar structures, for which the point-to-plane error metric [7] can provide strong constraints when surface normals are reliable [8]. In contrast, in open outdoor environments where points are farther apart and planar

<sup>†</sup>Corresponding author: Soohye Han

<sup>1</sup>Daehan Lee, Seongjun Kim, Soonbin Rho, Changhyeon Lee, Sanghyun Park, Junwoo Hong, Eunseon Choi, Hyunyoung Jo, and Soohye Han are with the Computational Control Engineering Laboratory (CoCEL), Department of Convergence IT Engineering and Electrical Engineering, Pohang University of Science and Technology (POSTECH), Pohang 37673, South Korea (email: soohye.han@postech.ac.kr)

<sup>2</sup>Hyungtae Lim is with the Laboratory for Information & Decision Systems (LIDS), Massachusetts Institute of Technology, Cambridge, MA 02139, USA

structure is weaker, surface normals tend to be less accurate, in which case the point-to-point error metric [9] can offer comparatively more reliable geometric constraints [8], [10]. Since these geometric characteristics can change as the robot moves, relying on a single residual type may reduce robustness across diverse scenes, as further discussed with experimental evidence in Sec. VI-E.

For these reasons, we seek a LIO framework that operates robustly and efficiently not only in indoor and outdoor environments but also during transitions between them. To this end, as presented in Fig. 1, we propose a generalizable LIO framework, called *GenZ-LIO*, designed around two guiding principles: (i) *robustness* to varying spatial scales and shifts in the dominant local geometric structure, and (ii) *computational efficiency* in correspondence search.

To achieve robustness, GenZ-LIO incorporates two scale- and geometry-aware mechanisms. First, it performs scale-aware adaptive voxelization, in which the voxel size is regulated via a feedback controller inspired by the principle of the proportional–integral–derivative (PID) controller, a widely used feedback control mechanism in control theory. The controller drives the voxelized point count toward a scene-scale-informed target derived from the current scan, with gains scheduled according to the estimated scene scale, the voxelized point count error, and its derivative, ensuring stable and responsive adaptation. Second, GenZ-LIO employs a hybrid-metric state update within an error-state iterated Kalman filter (ESIKF), adaptively combining point-to-plane [7] and point-to-point [9] residuals through reliability-based weighting informed by measurement uncertainty [11] and voxel discretization error [12].

To improve computational efficiency, we introduce a voxel-pruned correspondence search strategy to reduce the computational burden of point-to-point matching. In a voxel hash map, identifying a closest correspondence point typically requires examining up to 27 voxels around the query point [10], [12], which can incur considerable overhead. To avoid this brute-force traversal, our method first selects a compact subset of candidate voxels based on the query point’s location within the root voxel. During the subsequent search, we further prune candidate voxels by comparing the distance from the query point to each voxel with the current closest distance, skipping voxels that cannot yield a closer point. This two-stage pruning strategy prevents unnecessary voxel access and substantially improves correspondence search efficiency.

The main contributions of this paper are as follows. First, we propose GenZ-LIO, a generalizable LIO framework that operates robustly and efficiently across diverse scene scales, with performance validated through extensive experiments across indoor, outdoor, and transitional environments. To support evaluation under pronounced indoor–outdoor transitions, we also collect and publicly release a novel dataset acquired using custom hardware platforms encompassing scenarios with frequent and varied scene scale changes, together with the GenZ-LIO code.

In sum, we make the following five claims: (i) our system consistently achieves competitive odometry estimation performance across indoor, outdoor, and transitional environments;

(ii) our scale-aware adaptive voxelization enables robust state estimation while efficiently regulating computational resources by accounting for varying scene scales; (iii) our sensitivity-informed gain scheduling improves transient response, resulting in faster convergence and reduced overshoot and oscillations during voxel size control; (iv) our hybrid-metric state update mitigates LiDAR degeneracy caused by directionally insufficient planar constraints through the joint use of point-to-plane and point-to-point error metrics; (v) our voxel-pruned correspondence search substantially reduces computation time by pruning redundant traversal of neighboring voxels. These claims are backed up by the following sections and our experimental evaluation.

## II. RELATED WORK

In this section, we discuss two essential components of LiDAR-based odometry: (i) point cloud downsampling for efficient scan processing and (ii) error metrics for residual formulation in scan-to-map alignment.

Point cloud downsampling is an essential preprocessing step in LiDAR-based odometry to alleviate the computational and memory burden caused by the large volume of LiDAR data, which can reach hundreds of thousands to millions of points per second [6]. A common choice is uniform voxel grid sampling [13], [14], which discretizes space into fixed-sized cells (i.e., voxels) and retains a small number of points per voxel. This approach is simple to implement, computationally efficient, and integrates easily into existing front-end modules. For these reasons, it remains a common choice in state-of-the-art (SOTA) LiDAR(-inertial) odometry systems [6], [8], [10], [15]–[19]. As discussed in Sec. I, however, its reliance on a fixed voxel size makes it susceptible to substantial variations in scene scale.

To address the limitation of uniform voxel grid sampling, various point sampling approaches have been explored in LiDAR-based odometry to reduce redundancy or leverage informative measurements during optimization [20]–[25]. However, such approaches typically incur extra computational cost due to additional processing such as surface normal estimation. Moreover, they are commonly applied after an initial fixed-resolution voxelization of the raw scan, which may still expose them to the limitations of voxel grid sampling with a fixed voxel size.

In light of these considerations, adaptive voxel grid sampling schemes have been proposed to handle variations in scene scale while preserving real-time efficiency. Reinke *et al.* [3] introduced an adaptive scheme in LOCUS 2.0 that updates the voxel size to maintain a constant desired number of voxelized points  $N_{\text{desired}}^{\text{fixed}}$ , using a linear scaling strategy, as illustrated in Fig. 2(a). While this approach effectively regulates the voxelized point count to a user-defined level, it leaves room for further exploration on how the desired number of voxelized points should adapt in response to continuous variations in scene scale. Lim *et al.* [4] proposed AdaLIO, which switches between two pre-defined voxel sizes, as shown in Fig. 2(b). It uses a coarse voxel size  $d_{\text{coarse}}^{\text{fixed}}$  in general operation and switches to a fine voxel size  $d_{\text{fine}}^{\text{fixed}}$  when a

confined space is detected based on the number of voxelized points and the spatial distribution of occupied voxels. This approach can be effective when entering confined scenes, but its use of only two discrete, user-defined voxel sizes constrains continuous adaptation across a wide range of scene scales. More recently, Cheng *et al.* [5] proposed LIVOX-CAM, which adjusts the voxel size by first performing a temporary voxelization with a fixed voxel size  $d_{temp}^{fixed}$  and then updating it based on the ratio between the resulting and desired point counts; see Fig. 2(c). It updates the voxel size through a volume-based scaling strategy, unlike LOCUS 2.0 [3], which relies on a linear adjustment. Similar to LOCUS 2.0, LIVOX-CAM aims to maintain a fixed desired number of points  $N_{desired}^{fixed}$ , leaving open the question of how this target should adapt to continuous changes in scene scale.

In this study, we build on the computational efficiency and implementation simplicity of adaptive voxel grid sampling, while addressing key limitations of existing methods, including fixed target point counts [3], [5] and discrete voxel size switching [4]. In contrast to these approaches, our method explicitly estimates the scene scale using the scale indicator  $\bar{m}_t$  and determines a scale-informed target number of voxelized points  $N_{desired,t}$ . The voxel size is then regulated via a feedback controller with gain scheduling to drive the voxelized point count toward this target, enabling stable and responsive setpoint tracking under varying scene scales; see Fig. 2(d).

After downsampling the incoming LiDAR scan, the subsequent state estimation stage computes residuals from correspondences established between the current downsampled scan and a reference (another scan or a local submap) using various error metrics. Most SOTA LiDAR-inertial odometry systems typically adopt one of three widely used metric types: point-to-point [9], [12], point-to-plane [6], [7], [17], [26], [27], or generalized-ICP (G-ICP) [18], [19], [28]-based error metrics. For instance, Xu *et al.* [6] employed the point-to-plane metric in Fast-LIO2, an enhanced version of Fast-LIO [26] featuring direct matching, an ikd-Tree, and a novel Kalman gain formulation. Bai *et al.* [27] also utilized the point-to-plane metric in Faster-LIO, introducing parallel sparse incremental voxel updates for lightweight operation. Chen *et al.* [18] applied the G-ICP-based metric [29] in DLIO with continuous-time motion correction to mitigate distortion. He *et al.* [17] leveraged the point-to-plane metric in Point-LIO to perform state updates at every LiDAR point measurement. Wu *et al.* [12] adopted the point-to-point metric in LIO-EKF, employing adaptive thresholding for more robust data association. Chen *et al.* [19] integrated G-ICP-based constraints with inertial data in iG-LIO.

While these methods have demonstrated their effectiveness across various scenarios, relying solely on a single error metric can limit estimation accuracy depending on the geometrical characteristics of the surroundings [7], [8], [10]. For example, the point-to-point error metric [9] does not exploit planar information, and thus tends to be less accurate than the point-to-plane metric in structured environments [7], [8]. Conversely, the point-to-plane error metric [7] relies on estimated surface normals, which may become less reliable when LiDAR points are sparse or unstructured, potentially affecting alignment ac-

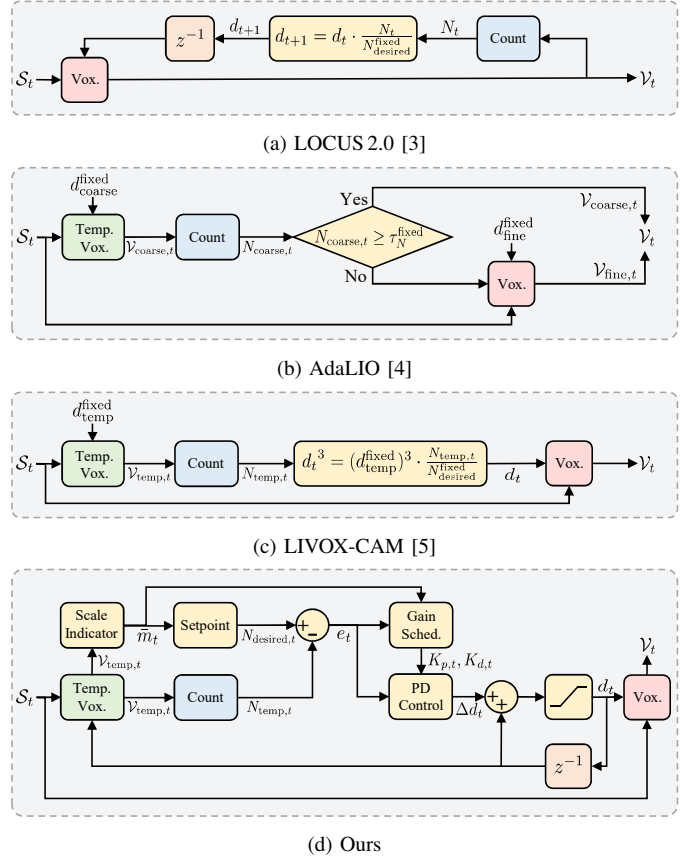


Fig. 2. Comparison of adaptive voxelization strategies. (a) LOCUS 2.0 [3] updates the voxel size for next scan, denoted by  $d_{t+1}$ , using the ratio of current voxelized point count  $N_t$  to the fixed desired point count  $N_{desired}^{fixed}$ . (b) AdaLIO [4] adaptively selects between pre-defined coarse voxel size  $d_{coarse}^{fixed}$  and the fine voxel size  $d_{fine}^{fixed}$  by checking whether the coarse voxelization yields fewer points than a fixed threshold  $\tau_N^{fixed}$ . (c) LIVOX-CAM [5] adjusts the voxel size  $d_t$  by first performing a temporary voxelization with a fixed voxel size  $d_{temp}^{fixed}$  and then updating it based on the ratio between the temporary point count  $N_{temp,t}$  and desired point count  $N_{desired}^{fixed}$ . This update follows a volume-based scaling strategy rather than a linear scaling in LOCUS 2.0 [3]. (d) Our method adaptively computes the desired point count  $N_{desired,t}$  based on the scale indicator  $\bar{m}_t$  and determines the corresponding voxel size  $d_t$  via proportional-derivative (PD) control with sensitivity-informed gain scheduling. This process corresponds to Fig. 3(b).

curacy [8], [10], [30]. Furthermore, rejecting correspondences associated with less reliable normals can reduce geometric constraints in certain directions, which may lead to pose drift, particularly in degenerate environments such as long corridors or open spaces [8], [24], [30]. Similarly, G-ICP [28] operates as a plane-to-plane error metric by assuming that all the surroundings are local planes. Under this formulation, however, it is also subject to the limitations of the point-to-plane metric, particularly when surface normals are unreliable or the local planar assumption does not hold, which may influence registration accuracy in certain scenarios [8].

To address the inherent limitations of individual error metrics, Lee *et al.* [8] revisit both the point-to-plane [7] and point-to-point [9] metrics, leveraging their complementary strengths in GenZ-ICP. Specifically, the point-to-plane error metric is applied to correspondences on structured surfaces where reliable surface normals can be estimated, while the point-to-point error metric is applied to correspondences in unstructured or sparse regions to avoid using unreliable normals. This

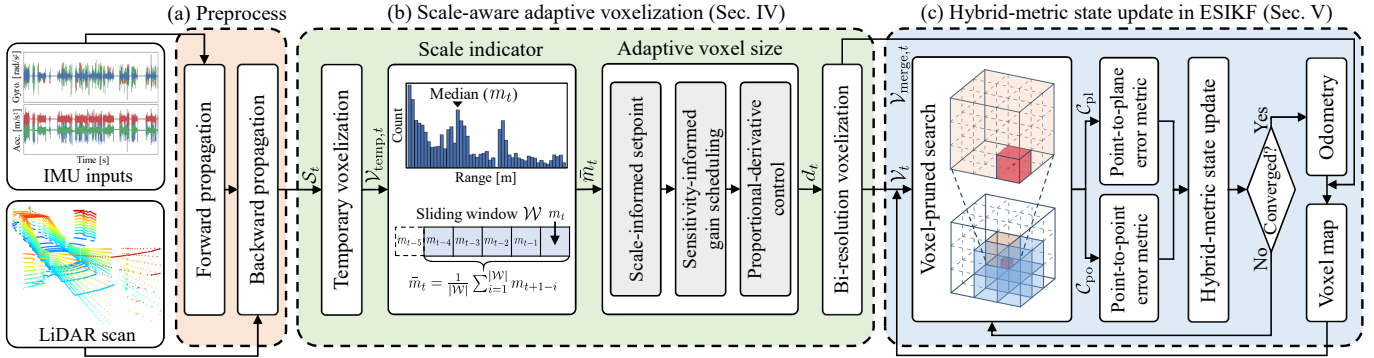


Fig. 3. System overview of *GenZ-LIO*. (a) In the preprocessing stage, forward propagation uses IMU measurements to propagate the state and covariance, and backward propagation removes motion distortion from the LiDAR scan, yielding the deskewed scan  $\mathcal{S}_t$ . (b) The scan  $\mathcal{S}_t$  is voxelized using the voxel size of previous timestep to produce the temporary voxelized scan  $\mathcal{V}_{\text{temp},t}$ . The median range  $m_t$  of points in  $\mathcal{V}_{\text{temp},t}$  is inserted into a sliding window to compute the scene scale indicator  $\bar{m}_t$ . Based on  $\bar{m}_t$ , a target number of voxelized points is set as a scale-informed control setpoint, and the voxel size  $d_t$  is adaptively adjusted via a PD controller with gain scheduling. The updated  $d_t$  is then used for bi-resolution voxelization of  $\mathcal{S}_t$ , yielding  $\mathcal{V}_{\text{merge},t}$  with  $d_t/2$  for map integration with reduced discretization error and  $\mathcal{V}_t$  with  $d_t$  for state update. (c) The voxelized scan  $\mathcal{V}_t$  is aligned with the voxel map for a voxel-pruned correspondence search, which avoids unnecessary traversal of neighboring voxels. This process produces the point-to-plane correspondence set  $\mathcal{C}_{\text{pl}}$  and point-to-point correspondence set  $\mathcal{C}_{\text{po}}$ , which are used in the hybrid-metric [8] state update. Finally, the transformed  $\mathcal{V}_{\text{merge},t}$  is integrated into the voxel map. For clarity, the control flow of the scale-aware adaptive voxelization is further illustrated in Fig. 2(d), where the bi-resolution voxelization step is omitted for comparison with other adaptive voxelization strategies.

adaptive metric selection improves robustness to geometric variation and mitigates optimization degradation by generating constraints along a broader range of directions.

However, *GenZ-ICP* assigns uniform weights to all correspondences of the same residual type, without accounting for the varying uncertainty of individual measurements. In this work, we address this limitation by extending the uncertainty-based weighting strategy of Yuan *et al.* [11], which was originally formulated for point-to-plane [7] correspondences. We additionally model the covariance of point-to-point [9] residuals and incorporate the variance of discretization error [12] to account for uncertainty induced by voxel-based map discretization. This formulation allows the optimization to prioritize more reliable observations while reducing the influence of noisy or uncertain measurements. That is, we adopt a state update that jointly uses point-to-plane [7] and point-to-point [9] metrics, which we refer to as a hybrid-metric state update. This hybrid-metric formulation mitigates LiDAR degeneracy under directionally insufficient planar constraints by jointly using point-to-plane and point-to-point error metrics.

### III. SYSTEM OVERVIEW

As illustrated by Fig. 3, *GenZ-LIO* is designed to provide robust and consistent odometry estimation across a wide range of scene scales, spanning both indoor and outdoor environments. To this end, the scale-aware adaptive voxelization module estimates the scene scale and determines the voxel size via a feedback controller with gain scheduling to drive the voxelized point count toward a scale-informed setpoint (Fig. 3(b)). Subsequently, the hybrid-metric state update is applied to mitigate the impact of directionally insufficient planar constraints, by jointly leveraging point-to-plane and point-to-point error metrics (Fig. 3(c)). During this procedure, point-to-point correspondence search can incur substantial computational overhead, and thus the voxel-pruned search strategy, which will be explained in Sec. V-B, is employed to avoid redundant computations without degrading odometry accuracy.

## IV. SCALE-AWARE ADAPTIVE VOXELIZATION

### A. Scale indicator

We begin by voxelizing the deskewed scan  $\mathcal{S}_t$  using the voxel size  $d_{t-1}$  from the previous timestep, resulting in a temporary voxelized scan  $\mathcal{V}_{\text{temp},t}$ , where  $d_0$  denotes the user-defined initial voxel size. To represent the spatial scale of the current scene, we first compute the range of each point in  $\mathcal{V}_{\text{temp},t}$  with respect to the LiDAR frame as  $\sqrt{x^2 + y^2 + z^2}$  and define the median of these ranges as  $m_t$ . Directly using the median range  $m_t$  as a scale indicator exhibits high-frequency variations due to scan-level fluctuations, making the subsequent voxel size adjustment overly sensitive. To mitigate this, we compute the smoothed median range  $\bar{m}_t = \frac{1}{|\mathcal{W}|} \sum_{i=1}^{|\mathcal{W}|} m_{t+1-i}$  by applying a moving average, where  $\mathcal{W}$  is a sliding window that stores up to  $N_w$  recent median ranges, and  $|\mathcal{W}|$  denotes the number of stored medians ( $|\mathcal{W}| \leq N_w$ ). The resulting  $\bar{m}_t$  serves as the scale indicator of the current scene.

As illustrated in Fig. 4, the scale indicator  $\bar{m}_t$  is proportional to the scene scale, yielding smaller values in confined indoor scenes (region A in Fig. 4) and larger values in open outdoor scenes (region B in Fig. 4). This property is used to determine the desired number of voxelized points in Sec. IV-C. Moreover, the scale indicator  $\bar{m}_t$ , together with tracking error-related terms, is used for gain scheduling in Sec. IV-E.

### B. Motivation for PID control in adaptive voxelization

Compared to narrow spaces, wide spaces typically require a larger number of points to preserve detailed geometric features of the environment. Accordingly, we aim to adjust the voxel size so that the voxelized point count is proportional to the scene scale. To this end, the desired number of voxelized points  $N_{\text{desired},t}$  is first determined from the scale indicator  $\bar{m}_t$ , and the voxel size is then adjusted to drive the voxelized point count toward this target  $N_{\text{desired},t}$ .

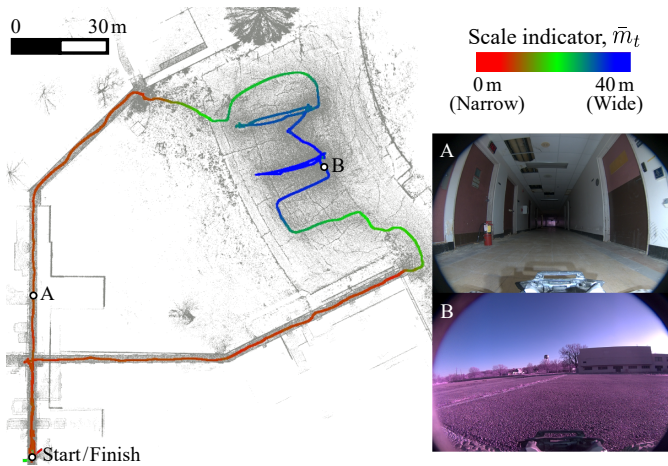


Fig. 4. Our scale indicator  $\bar{m}_t$  mapped onto the estimated trajectory for the Corridor 02 sequence of the SuperLoc [31] dataset, demonstrating its variation with the scene’s spatial scale.

However, the relationship between voxel size and the voxelized point count is scene-dependent and nonlinear; it evolves continuously as the scene changes and is difficult to model reliably in a closed form. This motivates the use of feedback control, and a PID controller provides a natural starting point for regulating the voxel size so that the voxelized point count tracks  $N_{\text{desired},t}$  through the proportional, integral, and derivative responses to tracking error.

In our case, however, the setpoint  $N_{\text{desired},t}$  is not fixed but varies over time with the scene scale (see Sec. IV-C). In such a time-varying setpoint tracking problem, the integral term can accumulate transient errors induced by setpoint changes and retain stale corrective actions, potentially leading to overshoot, oscillation, or delayed settling. Mitigating these effects while retaining the integral term would require additional mechanisms, such as conditional integration, anti-windup, or decay/reset strategies, together with extra user-defined parameters and increased tuning effort. Therefore, in view of these considerations, we adopt PD control in this work, retaining the proportional and derivative components while excluding the integral term. Based on this design choice, the components required for PD control are addressed in the following subsections: the control setpoint in Sec. IV-C, the tracking error and its derivative in Sec. IV-D, and gain scheduling in Sec. IV-E.

### C. Scale-informed setpoint

The scale-informed setpoint  $N_{\text{desired},t}$ , which serves as the control target, is defined as follows:

$$N_{\text{desired},t} = \begin{cases} N_{\min} + (N_{\max} - N_{\min}) \rho(\bar{m}_t), & \text{if } \bar{m}_t < \tau_m, \\ N_{\max}, & \text{otherwise,} \end{cases} \quad (1)$$

where  $N_{\min}$  and  $N_{\max}$  denote the user-defined lower and upper bounds of the desired number of voxelized points, respectively, and  $\tau_m$  is the threshold of the scale indicator beyond which  $N_{\text{desired},t}$  saturates at  $N_{\max}$ . The interpolation

function  $\rho(\bar{m}_t)$  is defined using a saturating power function as follows:

$$\rho(\bar{m}_t) = 1 - \left(1 - \frac{\bar{m}_t}{\tau_m}\right)^p, \quad p > 1, \quad (2)$$

which satisfies  $\rho(0) = 0$ ,  $\rho(\tau_m) = 1$ , and its first derivative satisfies  $\rho'(\tau_m) = 0$ . By enforcing a zero slope at the boundary  $\bar{m}_t = \tau_m$ , the setpoint  $N_{\text{desired},t}$  varies smoothly at the saturation point, avoiding abrupt derivative changes that could degrade the transient response of the proposed controller, such as unintended oscillations. The constant exponent  $p$  controls the growth rate of the setpoint, allowing the responsiveness of the setpoint evolution to be adjusted via a single parameter.

### D. Tracking error formulation

To track the scale-informed setpoint  $N_{\text{desired},t}$  in (1), we define the tracking error  $e_t$  and its derivative  $\Delta e_t$  for the PD controller as follows:

$$e_t = N_{\text{desired},t} - N_{\text{temp},t}, \quad \Delta e_t = \frac{e_t - e_{t-1}}{\Delta t_{\text{scan}}}, \quad (3)$$

where  $N_{\text{temp},t}$  is the number of points in the temporarily voxelized scan  $\mathcal{V}_{\text{temp},t}$ , and  $\Delta t_{\text{scan}}$  denotes the time interval between successive scans.

### E. Sensitivity-informed gain scheduling

Subsequently,  $e_t$  and  $\Delta e_t$  in (3) are input to the PD controller along with proportional and derivative gains,  $K_{p,t}$  and  $K_{d,t}$ , respectively. For linear systems, a standard PD controller with fixed gains can be sufficient. As discussed earlier, however, the relationship between voxel size and voxelized point count is nonlinear, meaning that fixed gains can lead to oscillations or delayed setpoint tracking; see Sec. VI-D.

For instance, in narrow and highly enclosed environments (i.e., low  $\bar{m}_t$ ), scan points are concentrated within a limited space, leading to high point density. Under such conditions, even small variations in voxel size can produce large changes in the voxelized point count. As a result, high gains tend to amplify overshoot and oscillations, making lower gains more suitable. Conversely, in wide and open environments (i.e., high  $\bar{m}_t$ ), scan points are distributed over a larger space, resulting in sparser point distributions. In this case, the voxelized point count is less sensitive to changes in voxel size, and higher gains are often required for more aggressive compensation. Therefore, the scale indicator  $\bar{m}_t$  can be used to infer the sensitivity of the voxelized point count to voxel size changes in the current scene and to adjust the control gains accordingly.

In addition to the scale indicator  $\bar{m}_t$ , the magnitudes of the tracking error  $|e_t|$  and its derivative  $|\Delta e_t|$  can also be determinants of gain selection. If the voxelized point count is already close to  $N_{\text{desired},t}$  (i.e., low  $|e_t|$ ), a smaller proportional gain promotes smoother tracking with reduced oscillation. When the tracking error is large (i.e., high  $|e_t|$ ), a larger proportional gain enables stronger compensation and faster setpoint tracking. Likewise, if the derivative magnitude  $|\Delta e_t|$  is small (i.e., low  $|\Delta e_t|$ ), a smaller derivative gain is sufficient because the tracking error is changing slowly. In contrast, when  $|\Delta e_t|$  is large (i.e., high  $|\Delta e_t|$ ), a larger derivative gain

helps damp rapid error variation, thereby reducing overshoot and oscillation.

Motivated by these observations, we propose a sensitivity-informed gain scheduling strategy in which the scale indicator  $\bar{m}_t$  is jointly considered with the tracking error magnitude  $|e_t|$  for the proportional gain  $K_{p,t}$ , and with the magnitude of the error derivative  $|\Delta e_t|$  for the derivative gain  $K_{d,t}$ . To this end, the scene scale indicator  $\bar{m}_t$  is normalized to  $\phi_t = \frac{\min(\bar{m}_t, \tau_m)}{\tau_m}$ . Similarly, the magnitudes of the tracking error  $|e_t|$  and its derivative  $|\Delta e_t|$  are normalized to  $\psi_{p,t}$  and  $\psi_{d,t}$ , respectively, as follows:

$$\begin{aligned}\psi_{p,t} &= \frac{\min(|e_t|, \lambda_p N_{\text{desired},t})}{\lambda_p N_{\text{desired},t}}, \\ \psi_{d,t} &= \frac{\min(|\Delta e_t|, \lambda_d N_{\text{desired},t}/\Delta t_{\text{scan}})}{\lambda_d N_{\text{desired},t}/\Delta t_{\text{scan}}},\end{aligned}\quad (4)$$

where  $\lambda_p \in (0, 1]$  and  $\lambda_d \in (0, 1]$  are empirically chosen scaling factors that compensate for the scale mismatch between the setpoint  $N_{\text{desired},t}$  in (1) and the magnitudes of the tracking error and its derivative in (3), respectively.

The interpolation factors  $\Gamma_{p,t}$  and  $\Gamma_{d,t}$  for the proportional and derivative gains, respectively, are then computed using the geometric mean of the corresponding normalized values as

$$\Gamma_{p,t} = \sqrt{\phi_t \cdot \psi_{p,t}}, \quad \Gamma_{d,t} = \sqrt{\phi_t \cdot \psi_{d,t}}. \quad (5)$$

These interpolation factors are used to determine the proportional and derivative gains as follows:

$$\begin{aligned}K_{p,t} &= K_{p,\min} + (K_{p,\max} - K_{p,\min}) \Gamma_{p,t}, \\ K_{d,t} &= K_{d,\min} + (K_{d,\max} - K_{d,\min}) \Gamma_{d,t},\end{aligned}\quad (6)$$

where  $K_{p,\min}$ ,  $K_{p,\max}$ ,  $K_{d,\min}$ , and  $K_{d,\max}$  denote user-defined gain bounds.

Through the geometric mean, the proposed gain scheduling incorporates both the scale indicator and the corresponding error-related magnitude into each gain. For the proportional gain, consider a narrow scene (i.e., low  $\phi_t$ ) with large tracking error (i.e., high  $\psi_{p,t}$ ). If only the scene scale were considered, the resulting gain would remain low, leading to slow compensation. Conversely, if only the tracking error magnitude were considered, the resulting gain could become excessively high, potentially inducing oscillations in narrow scenes where the voxelized point count is highly sensitive to small changes in voxel size. By accounting for both  $\phi_t$  and  $\psi_{p,t}$ ,  $\Gamma_{p,t}$  yields a proportional gain that is higher than that based on scene scale alone, promoting faster compensation, yet lower than that based on tracking error magnitude alone, mitigating oscillations.

A similar rationale applies to the derivative gain. In narrow scenes, using only the scene scale would keep the derivative gain low even when the error derivative is large, thereby weakening damping against rapid error variation. Conversely, using only the derivative magnitude could produce an excessively large derivative gain, which may overreact to transient fluctuations. By jointly accounting for  $\phi_t$  and  $\psi_{d,t}$ ,  $\Gamma_{d,t}$  adjusts the derivative gain in a balanced manner, strengthening damping when the error changes rapidly while avoiding unnecessarily aggressive responses in highly sensitive scenes.

---

### Algorithm 1: Scale-aware adaptive voxelization

---

**Input** : Deskewed scan  $\mathcal{S}_t$ ; previous voxel size  $d_{t-1}$ ;  
previous tracking error  $e_{t-1}$ ; scan interval  $\Delta t_{\text{scan}}$ ; voxel size bounds  $[d_{\min}, d_{\max}]$ ;  
window size  $N_w$ ; point count bounds  $[N_{\min}, N_{\max}]$ ; scene scale threshold  $\tau_m$ ;  
scaling factors  $\lambda_p, \lambda_d$ ; exponent  $p$ ; gain bounds  $[K_{p,\min}, K_{p,\max}], [K_{d,\min}, K_{d,\max}]$ .

**Output**: Voxelized scans  $\mathcal{V}_t, \mathcal{V}_{\text{merge},t}$ .

```

1 // Scale indicator
2  $\mathcal{V}_{\text{temp},t} \leftarrow \text{Voxelize}(\mathcal{S}_t, d_{t-1})$ ;
3  $N_{\text{temp},t} \leftarrow \text{Count}(\mathcal{V}_{\text{temp},t})$ ;
4 Let  $R = \{\|\mathbf{p}_i\| \mid \mathbf{p}_i \in \mathcal{V}_{\text{temp},t}\}$ ;
5  $m_t \leftarrow \text{median}(R)$ ;
6 Append  $m_t$  to window  $\mathcal{W}$ ; if  $|\mathcal{W}| > N_w$  then
7   remove oldest element from  $\mathcal{W}$ ;
8  $\bar{m}_t \leftarrow \frac{1}{|\mathcal{W}|} \sum_{i=1}^{|\mathcal{W}|} m_{t+1-i}$ ;
9 // Scale-informed setpoint
10 if  $\bar{m}_t \geq \tau_m$  then
11    $N_{\text{desired},t} \leftarrow N_{\max}$ ;
12 else
13    $\rho(\bar{m}_t) \leftarrow 1 - \left(1 - \frac{\bar{m}_t}{\tau_m}\right)^p$ ;
14    $N_{\text{desired},t} \leftarrow N_{\min} + (N_{\max} - N_{\min}) \rho(\bar{m}_t)$ ;
15 // Tracking error formulation
16  $e_t \leftarrow N_{\text{desired},t} - N_{\text{temp},t}$ ;
17  $\Delta e_t \leftarrow (e_t - e_{t-1})/\Delta t_{\text{scan}}$ ;
18 // Sensitivity-informed gain scheduling
19  $\phi_t \leftarrow \frac{\min(\bar{m}_t, \tau_m)}{\tau_m}$ ;
20  $\psi_{p,t} \leftarrow \frac{\min(|e_t|, \lambda_p N_{\text{desired},t})}{\lambda_p N_{\text{desired},t}}$ ;
21  $\psi_{d,t} \leftarrow \frac{\min(|\Delta e_t|, \lambda_d N_{\text{desired},t}/\Delta t_{\text{scan}})}{\lambda_d N_{\text{desired},t}/\Delta t_{\text{scan}}}$ ;
22  $\Gamma_{p,t} \leftarrow \sqrt{\phi_t \cdot \psi_{p,t}}$ ;
23  $\Gamma_{d,t} \leftarrow \sqrt{\phi_t \cdot \psi_{d,t}}$ ;
24  $K_{p,t} \leftarrow K_{p,\min} + (K_{p,\max} - K_{p,\min}) \Gamma_{p,t}$ ;
25  $K_{d,t} \leftarrow K_{d,\min} + (K_{d,\max} - K_{d,\min}) \Gamma_{d,t}$ ;
26 // Voxel size update
27  $\Delta d_t \leftarrow -K_{p,t} e_t - K_{d,t} \Delta e_t$ ;
28  $d_t \leftarrow \text{clamp}(d_{t-1} + \Delta d_t, d_{\min}, d_{\max})$ ;
29  $e_{t-1} \leftarrow e_t$ ;
30 // Bi-resolution voxelization
31  $\mathcal{V}_{\text{merge},t} \leftarrow \text{Voxelize}(\mathcal{S}_t, d_t/2)$ ;
32  $\mathcal{V}_t \leftarrow \text{Voxelize}(\mathcal{V}_{\text{merge},t}, d_t)$ ;
33 return  $\mathcal{V}_t, \mathcal{V}_{\text{merge},t}$ .
```

---

Following the PD control law, the voxel size adjustment  $\Delta d_t$  is computed using  $K_{p,t}$  and  $K_{d,t}$  in (6) as follows:

$$\Delta d_t = -K_{p,t} e_t - K_{d,t} \Delta e_t. \quad (7)$$

The negative signs in both terms reflect the inverse relationship between voxelized point count and voxel size. When the error is positive, which indicates that  $N_{\text{temp},t}$  is lower than

$N_{\text{desired},t}$ , the voxel size needs to be decreased to increase the point count. The voxel size is then updated as follows:

$$d_t = \text{clamp}(d_{t-1} + \Delta d_t, d_{\min}, d_{\max}), \quad (8)$$

where  $\text{clamp}(\cdot, \cdot, \cdot)$  constrains  $d_t$  to the user-defined interval  $[d_{\min}, d_{\max}]$  to prevent the voxelized scan from becoming excessively sparse or dense.

#### F. Bi-resolution voxelization

Next,  $d_t$  in (8) is used in a bi-resolution voxelization, which is widely adopted from existing LiDAR-based odometry approaches [10], [15] to reduce discretization errors by retaining higher density in map update scans. First, the current LiDAR scan  $\mathcal{S}_t$  is voxelized with  $d_t/2$  to produce  $\mathcal{V}_{\text{merge},t}$  for map update. Then,  $\mathcal{V}_{\text{merge},t}$  is re-voxelized using  $d_t$  to obtain  $\mathcal{V}_t$ , which is used for state update, as illustrated in Fig. 3.

In summary, the proposed scale-aware adaptive voxelization adjusts the voxel size according to the scene scale, improving the robustness and computational efficiency of LiDAR-based odometry across a wide range of scene scales; see Secs. VI-B and VI-C. Moreover, the proposed sensitivity-informed gain scheduling strategy mitigates oscillations in voxel size control and enables improved stability and responsiveness in tracking the scale-informed setpoint; see Sec. VI-D. Algorithm 1 details the proposed method, and Fig. 2 further contrasts it with other adaptive voxelization strategies [3]–[5] through control flow diagrams.

### V. HYBRID-METRIC STATE UPDATE IN ERROR-STATE ITERATED KALMAN FILTER

The voxelized scan  $\mathcal{V}_t$  is used for correspondence search, residual computation, and state update, as illustrated in Fig. 3(c). Before detailing the state update procedure, the notations and assumptions are summarized in Sec. V-A. The voxel-pruned correspondence search is then described in Sec. V-B, the residual formulation and associated Jacobians and covariances are presented in Secs. V-C and V-D, and the hybrid-metric state update is detailed in Sec. V-E.

#### A. Assumptions and notations

The system employs a tightly coupled LiDAR–IMU configuration with a known temporal offset obtained through prior calibration or synchronization. The IMU frame, denoted as  $I$ , is adopted as the body frame, and the initial body frame is aligned with the global world frame  $W$ . The LiDAR and IMU are rigidly mounted, with their extrinsic transformation pre-calibrated. The notations used in the ESIKF are summarized in Table I. Although this section primarily focuses on the hybrid-metric state update (i.e., correction step), we briefly review the prediction step of the ESIKF [6], [32] to introduce the state variables and notations used in the subsequent derivations.

The discrete state transition model associated with the  $i$ -th IMU measurement is given by:

$$\mathbf{x}_{i+1} = \mathbf{x}_i \boxplus (\Delta t_{\text{imu}} f(\mathbf{x}_i, \mathbf{u}_i, \mathbf{w}_i)), \quad (9)$$

TABLE I. Some important notations in an error-state iterated Kalman filter.

Notation	Explanation
$\boxplus / \boxminus$	The encapsulated “boxplus” and “boxminus” operations on the state manifold
$W(\cdot)$	A vector $(\cdot)$ in global world frame
$L(\cdot)$	A vector $(\cdot)$ in LiDAR frame
${}^I\mathbf{T}_L$	The extrinsic of the LiDAR frame w.r.t. the IMU frame
${}^W\mathbf{T}_I$	The pose of the IMU frame w.r.t. the world frame
$\mathbf{x}, \hat{\mathbf{x}}, \tilde{\mathbf{x}}$	The ground truth, propagated and updated estimation of $\mathbf{x}$
$\tilde{\mathbf{x}}^\ell$	The $\ell$ -th update of $\tilde{\mathbf{x}}$
$\tilde{\mathbf{x}}$	The error state between ground truth $\mathbf{x}$ and its estimate $\hat{\mathbf{x}}$

where  $\Delta t_{\text{imu}}$  is the IMU sampling period. The state manifold  $\mathcal{M}$ , state  $\mathbf{x}$ , IMU input  $\mathbf{u}$ , process noise  $\mathbf{w}$ , and system function  $f(\cdot, \cdot, \cdot)$  are defined as follows:

$$\begin{aligned} \mathcal{M} &\triangleq SO(3) \times \mathbb{R}^{15}, \quad \dim(\mathcal{M}) = 18, \\ \mathbf{x} &\triangleq [{}^W\mathbf{t}_I^\top \quad {}^W\mathbf{R}_I^\top \quad {}^W\mathbf{v}_I^\top \quad \mathbf{b}_g^\top \quad \mathbf{b}_a^\top \quad {}^W\mathbf{g}^\top]^\top \in \mathcal{M}, \\ \mathbf{u} &\triangleq [\boldsymbol{\omega}_m^\top \quad \mathbf{a}_m^\top]^\top, \quad \mathbf{w} \triangleq [\boldsymbol{\delta}_g^\top \quad \boldsymbol{\delta}_a^\top \quad \boldsymbol{\delta}_{\mathbf{b}_g}^\top \quad \boldsymbol{\delta}_{\mathbf{b}_a}^\top]^\top, \\ f(\mathbf{x}, \mathbf{u}, \mathbf{w}) &= \begin{bmatrix} {}^W\mathbf{v}_I + \frac{1}{2}({}^W\mathbf{R}_I(\mathbf{a}_m - \mathbf{b}_a - \boldsymbol{\delta}_a) + {}^W\mathbf{g})\Delta t_{\text{imu}} \\ \boldsymbol{\omega}_m - \mathbf{b}_g - \boldsymbol{\delta}_g \\ {}^W\mathbf{R}_I(\mathbf{a}_m - \mathbf{b}_a - \boldsymbol{\delta}_a) + {}^W\mathbf{g} \\ \boldsymbol{\delta}_{\mathbf{b}_g} \\ \boldsymbol{\delta}_{\mathbf{b}_a} \\ \mathbf{0}_{3 \times 1} \end{bmatrix}, \end{aligned} \quad (10)$$

where  ${}^W\mathbf{t}_I$ ,  ${}^W\mathbf{R}_I$ , and  ${}^W\mathbf{v}_I$  represent the IMU position, attitude, and velocity in the world frame, respectively,  ${}^W\mathbf{g}$  is the gravity vector in the world frame,  $\boldsymbol{\omega}_m$  and  $\mathbf{a}_m$  are the measured angular velocity and linear acceleration with associated noises  $\boldsymbol{\delta}_g$  and  $\boldsymbol{\delta}_a$ , respectively, and  $\mathbf{b}_g$  and  $\mathbf{b}_a$  are IMU bias modeled as random walks driven by Gaussian noise  $\boldsymbol{\delta}_{\mathbf{b}_g}$  and  $\boldsymbol{\delta}_{\mathbf{b}_a}$ , respectively.

The state and covariance are propagated over the duration of a LiDAR scan using the available IMU measurements. During this interval, forward propagation predicts the state at each IMU input  $\mathbf{u}_i$  by setting the process noise  $\mathbf{w}_i$  in (9) to zero. Let  $\tilde{\mathbf{x}}$  and  $\hat{\mathbf{P}}$  denote the propagated state and covariance, respectively, which are used as the prior for the subsequent update step as follows:

$$\tilde{\mathbf{x}} = \mathbf{x} \boxplus \tilde{\mathbf{x}} \sim \mathcal{N}(\mathbf{0}, \hat{\mathbf{P}}), \quad (11)$$

where the error state  $\tilde{\mathbf{x}}$  corresponds to the state  $\mathbf{x}$  in (10) and is expressed as follows:

$$\tilde{\mathbf{x}} = [\boldsymbol{\delta}_{w_{\mathbf{t}_I}}^\top, \boldsymbol{\delta}_{w_{\mathbf{r}_I}}^\top, \boldsymbol{\delta}_{w_{\mathbf{v}_I}}^\top, \boldsymbol{\delta}_{\mathbf{b}_g}^\top, \boldsymbol{\delta}_{\mathbf{b}_a}^\top, \boldsymbol{\delta}_{w_{\mathbf{g}}}^\top]^\top \in \mathbb{R}^{18 \times 1}. \quad (12)$$

#### B. Voxel-pruned correspondence search

The voxelized scan  $\mathcal{V}_t$  obtained from Sec. IV-F is first transformed into the world frame using the pose prior for scan-to-map matching. At this stage, to establish point-to-plane and point-to-point correspondences in a computationally efficient manner, we propose a voxel-pruned correspondence search that prunes unnecessary traversal of neighboring voxels.

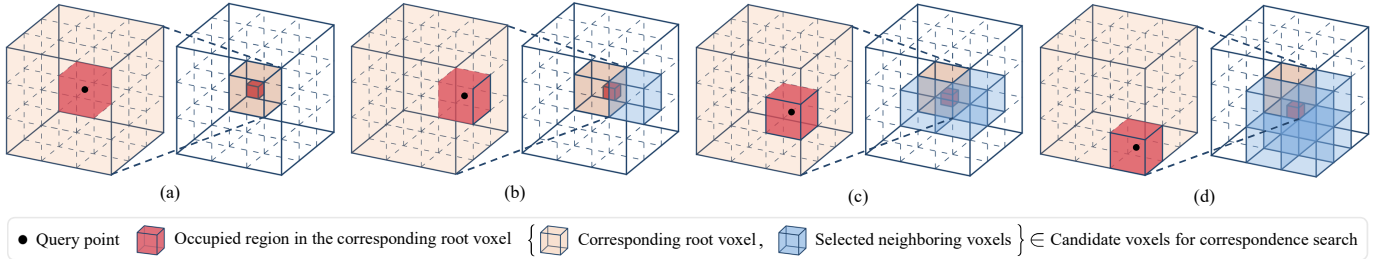


Fig. 5. Candidate voxel selection based on the region occupied by a query point within its corresponding root voxel. The root voxel is divided into 27 regions, and the occupied region falls into one of four cases: (a) center case, selecting no neighboring voxel; (b) surface case, selecting one surface-sharing neighboring voxel; (c) edge case, selecting three edge-sharing neighboring voxels; and (d) corner case, selecting seven corner-sharing neighboring voxels. The selected neighboring voxels, together with the root voxel, are considered candidate voxels for correspondence search. In Algorithm 2, the function `GetCandidateVoxels` selects the candidate voxels based on these sharing relations.

1) *Candidate voxel selection*: Given a query point  ${}^W\mathbf{p}$  from the transformed  $\mathcal{V}_t$ , the voxel map [11] is queried to identify the corresponding root voxel that contains  ${}^W\mathbf{p}$ . Subsequently, correspondence search is performed over the root voxel and its neighboring voxels to find a point-to-plane or point-to-point correspondence. In this process, we first determine a set of candidate voxels to visit for correspondence search. That is, instead of performing a brute-force search over all 26 neighboring voxels of the root voxel [10], [12], we adaptively select only those neighboring voxels that can plausibly contain a valid correspondence, based on the position of the query point within the root voxel.

To this end, as illustrated in Fig. 5, the root voxel, shown as a zoomed-in light orange voxel, is conceptually partitioned into 27 regions to determine the relative location of the query point within the voxel. The occupied region of the query point is categorized into one of four cases—center, surface, edge, or corner—each corresponding to a distinct sharing relation with neighboring voxels. Based on this classification, the root voxel and only a subset of neighboring voxels that share a face, edge, or corner with the occupied region are selected as candidate voxels for correspondence search. For example, when the query point lies in a corner region of the root voxel, as shown in Fig. 5(d), the root voxel and seven corner-sharing neighboring voxels are selected, resulting in eight candidate voxels in total.

2) *Point-to-plane correspondence search*: Correspondence search is then performed over the candidate voxels selected above. Each voxel stores an estimated normal vector  ${}^W\mathbf{n}$ , a centroid  ${}^W\mathbf{q}$ , and a set of accumulated points  $\mathcal{P} = \{{}^W\mathbf{p}'_j\}_{j=1}^{N_{\text{stored}}}$  from past observations, where  ${}^W\mathbf{p}'_j$  denotes a stored past observation point expressed in the world frame, and  $N_{\text{stored}}$  is the number of stored points per voxel, upper-bounded by a user-defined maximum. Point-to-plane matching directly leverages the stored normal and centroid and can therefore be evaluated at low computational cost. Accordingly, we first attempt to establish a point-to-plane correspondence.

Using the stored normal and centroid, candidate point-to-plane correspondences are evaluated over the selected voxels with a statistical gating test based on the  $3\sigma$  criterion [11]. If multiple candidate planes satisfy the criterion, the plane with the highest matching probability is selected as the final point-to-plane correspondence [11]. This correspondence is then inserted into the point-to-plane correspondence set  $\mathcal{C}_{\text{pl}}$ .

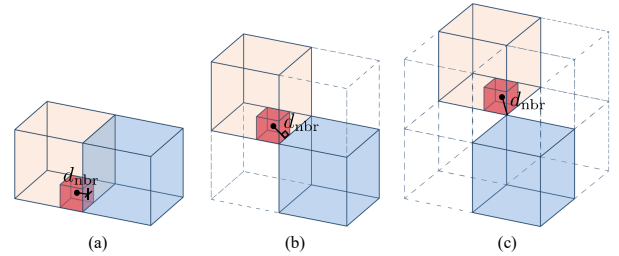


Fig. 6. Definition of the distance  $d_{\text{nbr}}$  between a query point and selected neighboring voxels. In Fig. 5, the distance from the query point to a selected neighboring voxel falls into one of three categories: (a) point-to-surface distance (surface-sharing relation); (b) point-to-edge distance (edge-sharing relation); and (c) point-to-corner distance (corner-sharing relation). In Algorithm 2, the function `ComputeDistanceToVoxel` determines the distance type based on these sharing relations between the query point's occupied region and the selected neighboring voxel.

3) *Point-to-point correspondence search with additional voxel pruning*: When no valid point-to-plane correspondence is found, the algorithm falls back to point-to-point correspondence search rather than discarding the query point. Compared with using only point-to-plane correspondences, this fallback helps form geometric constraints in more diverse directions, thereby mitigating degeneracy in the optimization [8]; see Sec. VI-E.

However, unlike point-to-plane matching, point-to-point matching requires computing Euclidean distances to all stored points within candidate voxels to identify the closest correspondence, which can incur substantial computational overhead. For this reason, we propose an additional pruning strategy, which skips candidate neighboring voxels that cannot yield a closer point than the current best one.

We first define the minimum distance from the query point to a candidate neighboring voxel, denoted by  $d_{\text{nbr}}$ . As illustrated in Fig. 6,  $d_{\text{nbr}}$  is determined by the sharing relation between the query point's occupied region within the root voxel and the neighboring voxel. Specifically, it corresponds to a point-to-surface, point-to-edge, or point-to-corner distance when the neighboring voxel shares a surface, edge, or corner with the occupied region, respectively.

With this definition, the search first evaluates the root voxel and obtains the distance to the closest point found so far, denoted by  $d_{\text{closest}}$ . For each candidate neighboring voxel, a coarse-to-fine check is applied:  $d_{\text{nbr}}$  is first computed as the minimum distance from the query point to the voxel itself, without accessing any stored points. Since no stored

---

**Algorithm 2:** Pruning strategy for point-to-point correspondence search

---

**Input :** Transformed query point  ${}^W\mathbf{p}$ ; fixed root voxel size  $d_{\text{root}}$ ; outlier rejection threshold  $\tau_{\text{closest}}$ .

**Output:** Nearest point  ${}^W\hat{\mathbf{p}}$  and its distance  $d_{\text{closest}}$ .

- 1  $(\mathcal{V}_{\text{root}}, \mathcal{V}_{\text{nbrs}}) \leftarrow \text{GetCandidateVoxels}({}^W\mathbf{p}, d_{\text{root}})$ ;
- 2  $d_{\text{closest}} \leftarrow \tau_{\text{closest}}$ ;
- 3  $({}^W\hat{\mathbf{p}}_{\text{temp}}, d_{\text{temp}}) \leftarrow \text{NN-Search}(\mathcal{V}_{\text{root}}, {}^W\mathbf{p})$ ;
- 4 **if**  $d_{\text{temp}} < d_{\text{closest}}$  **then**
- 5    $\lfloor ({}^W\hat{\mathbf{p}}, d_{\text{closest}}) \leftarrow ({}^W\hat{\mathbf{p}}_{\text{temp}}, d_{\text{temp}})$ ;
- 6 **for**  $\mathcal{V}_{\text{nbr}} \in \mathcal{V}_{\text{nbrs}}$  **do**
- 7    $d_{\text{nbr}} \leftarrow \text{ComputeDistanceToVoxel}({}^W\mathbf{p}, \mathcal{V}_{\text{nbr}})$ ;
- 8   **if**  $d_{\text{nbr}} < d_{\text{closest}}$  **then**
- 9      $({}^W\hat{\mathbf{p}}_{\text{temp}}, d_{\text{temp}}) \leftarrow \text{NN-Search}(\mathcal{V}_{\text{nbr}}, {}^W\mathbf{p})$ ;
- 10    **if**  $d_{\text{temp}} < d_{\text{closest}}$  **then**
- 11      $\lfloor ({}^W\hat{\mathbf{p}}, d_{\text{closest}}) \leftarrow ({}^W\hat{\mathbf{p}}_{\text{temp}}, d_{\text{temp}})$ ;
- 12 **if**  $d_{\text{closest}} < \tau_{\text{closest}}$  **then**
- 13    $\lfloor$  **return**  $({}^W\hat{\mathbf{p}}, d_{\text{closest}})$ ;
- 14 **else**
- 15    $\lfloor$  **return**  $\emptyset$ .

---

point inside that voxel can be closer than  $d_{\text{nbr}}$ , the voxel is skipped if  $d_{\text{nbr}} \geq d_{\text{closest}}$ ; otherwise, a point-level nearest-neighbor search is performed within that voxel. Note that  $d_{\text{closest}}$  is initialized with an outlier rejection threshold  $\tau_{\text{closest}}$  to discard correspondences that are excessively distant from the query point. The detailed pruning procedure is summarized in Algorithm 2.

If a valid closest point is found, it is inserted into the point-to-point correspondence set  $\mathcal{C}_{\text{po}}$ . If neither a valid point-to-plane nor a valid point-to-point correspondence is found, the query point is regarded as a noise-induced outlier and excluded from further processing. The above procedures are performed independently for each query point in the transformed  $\mathcal{V}_t$ , resulting in two correspondence sets: the point-to-plane set  $\mathcal{C}_{\text{pl}}$  and the point-to-point set  $\mathcal{C}_{\text{po}}$ . The correspondences in  $\mathcal{C}_{\text{pl}}$  are used to compute point-to-plane residuals, Jacobians, and covariances in Sec. V-C, while those in  $\mathcal{C}_{\text{po}}$  are used to compute point-to-point residuals, Jacobians, and covariances in Sec. V-D.

### C. Setting point-to-plane residual, Jacobian, and covariance

For each correspondence in the point-to-plane set  $\mathcal{C}_{\text{pl}}$ , the point-to-plane error metric [7] is applied. The normal  ${}^W\mathbf{n}$ , center  ${}^W\mathbf{q}$ , and query point  ${}^L\mathbf{p}$  are accompanied by noise terms  $\delta_{w_{\mathbf{n}}}$ ,  $\delta_{w_{\mathbf{q}}}$ , and  $\delta_{L_{\mathbf{p}}}$ , respectively. Considering these noise terms jointly, the point-to-plane measurement model  $\mathbf{h}_{\text{pl}}(\mathbf{x}, \mathbf{v}_{\text{pl}})$  can be expressed as follows:

$$0 = \mathbf{h}_{\text{pl}}(\mathbf{x}, \mathbf{v}_{\text{pl}}) \triangleq ({}^W\mathbf{n} \boxplus \delta_{w_{\mathbf{n}}})^\top ({}^W\mathbf{T}_I {}^I\mathbf{T}_L ({}^L\mathbf{p} + \delta_{L_{\mathbf{p}}}) - {}^W\mathbf{q} - \delta_{w_{\mathbf{q}}}), \quad (13)$$

where the point-to-plane noise vector  $\mathbf{v}_{\text{pl}}$  is defined as follows:

$$\mathbf{v}_{\text{pl}} = [\delta_{w_{\mathbf{n}}}^\top, \delta_{w_{\mathbf{q}}}^\top, \delta_{L_{\mathbf{p}}}^\top]^\top \in \mathbb{R}^{9 \times 1}. \quad (14)$$

Note that the state estimate at the  $\ell$ -th iteration is denoted by  $\hat{\mathbf{x}}^\ell$ , where  $\hat{\mathbf{x}}^\ell = \hat{\mathbf{x}}$ . To compute the residual, Jacobian, and covariance, the point-to-plane measurement model (13) is linearized at  $\hat{\mathbf{x}}^\ell$  using a first-order Taylor expansion, as follows:

$$0 \simeq z_{\text{pl}}^\ell + \mathbf{H}_{\hat{\mathbf{x}}, \text{pl}}^\ell \tilde{\mathbf{x}}^\ell + \mathbf{H}_{\mathbf{v}, \text{pl}}^\ell \mathbf{v}_{\text{pl}}, \quad (15)$$

where  $z_{\text{pl}}^\ell (= \mathbf{h}_{\text{pl}}(\hat{\mathbf{x}}^\ell, \mathbf{0}))$  is the point-to-plane residual,  $\tilde{\mathbf{x}}^\ell = \mathbf{x} \boxminus \hat{\mathbf{x}}^\ell$ ,  $\mathbf{H}_{\mathbf{v}, \text{pl}}^\ell \mathbf{v}_{\text{pl}} \sim \mathcal{N}(0, R_{\text{pl}}^\ell)$  is the lumped point-to-plane measurement noise,  $\mathbf{H}_{\hat{\mathbf{x}}, \text{pl}}^\ell$  and  $\mathbf{H}_{\mathbf{v}, \text{pl}}^\ell$  are the Jacobian matrices of  $\mathbf{h}_{\text{pl}}(\hat{\mathbf{x}}^\ell \boxplus \tilde{\mathbf{x}}^\ell, \mathbf{v}_{\text{pl}})$  with respect to  $\tilde{\mathbf{x}}^\ell$  and  $\mathbf{v}_{\text{pl}}$ , evaluated at zero, respectively.  $z_{\text{pl}}^\ell \in \mathbb{R}$ ,  $\mathbf{H}_{\hat{\mathbf{x}}, \text{pl}}^\ell \in \mathbb{R}^{1 \times 18}$  and  $\mathbf{H}_{\mathbf{v}, \text{pl}}^\ell \in \mathbb{R}^{1 \times 9}$  are expressed as follows:

$$\begin{aligned} z_{\text{pl}}^\ell &= {}^W\mathbf{n}^\top ({}^W\mathbf{T}_I {}^I\mathbf{T}_L {}^L\mathbf{p} - {}^W\mathbf{q}), \\ \mathbf{H}_{\hat{\mathbf{x}}, \text{pl}}^\ell &= [{}^W\mathbf{n}^\top, -{}^W\mathbf{n}^\top {}^W\mathbf{R}_I {}^I\mathbf{R}_L [{}^L\mathbf{p}]_\times, \mathbf{0}_{1 \times 12}], \\ \mathbf{H}_{\mathbf{v}, \text{pl}}^\ell &= [({}^W\mathbf{T}_I {}^I\mathbf{T}_L {}^L\mathbf{p} - {}^W\mathbf{q})^\top, -{}^W\mathbf{n}^\top, {}^W\mathbf{n}^\top {}^W\mathbf{R}_I {}^I\mathbf{R}_L], \end{aligned} \quad (16)$$

where  $[\cdot]_\times$  is an operator that converts the 3D vector into a skew-symmetric matrix.

Thus, (15) can be reformulated as follows:

$$z_{\text{pl}}^\ell + \mathbf{H}_{\hat{\mathbf{x}}, \text{pl}}^\ell \tilde{\mathbf{x}}^\ell \simeq -\mathbf{H}_{\mathbf{v}, \text{pl}}^\ell \mathbf{v}_{\text{pl}} \sim \mathcal{N}(0, R_{\text{pl}}^\ell), \quad (17)$$

where the point-to-plane covariance  $R_{\text{pl}}^\ell$  is defined as

$$R_{\text{pl}}^\ell = \mathbf{H}_{\mathbf{v}, \text{pl}}^\ell \Sigma_{w_{\mathbf{n}}, w_{\mathbf{q}}, L_{\mathbf{p}}} \mathbf{H}_{\mathbf{v}, \text{pl}}^{\ell \top} \in \mathbb{R}. \quad (18)$$

Here, the noise covariance  $\Sigma_{w_{\mathbf{n}}, w_{\mathbf{q}}, L_{\mathbf{p}}}$  is given by

$$\Sigma_{w_{\mathbf{n}}, w_{\mathbf{q}}, L_{\mathbf{p}}} = \begin{bmatrix} \Sigma_{w_{\mathbf{n}}, w_{\mathbf{q}}} & \mathbf{0}_{6 \times 3} \\ \mathbf{0}_{3 \times 6} & \Sigma_{L_{\mathbf{p}}} \end{bmatrix} \in \mathbb{R}^{9 \times 9}, \quad (19)$$

where  $\Sigma_{w_{\mathbf{n}}, w_{\mathbf{q}}}$  denotes the covariance of the normal  ${}^W\mathbf{n}$  and center  ${}^W\mathbf{q}$ , and  $\Sigma_{L_{\mathbf{p}}}$  denotes the covariance of the query point  ${}^L\mathbf{p}$  in the LiDAR frame. Detailed derivations of these terms are provided in Yuan *et al.* [11].

This procedure is applied to all elements of  $\mathcal{C}_{\text{pl}}$  (i.e., point-to-plane correspondences) to obtain the point-to-plane residuals  $z_{\text{pl}}^\ell$ , Jacobians  $\mathbf{H}_{\hat{\mathbf{x}}, \text{pl}}^\ell$ , and covariances  $R_{\text{pl}}^\ell$  for each correspondence. These terms are then used in the hybrid-metric state update described in Sec. V-E.

### D. Setting point-to-point residual, Jacobian, and covariance

Next, for each correspondence in the point-to-point set  $\mathcal{C}_{\text{po}}$ , the point-to-point error metric [9] is applied. As with (13), the point-to-point measurement model  $\mathbf{h}_{\text{po}}(\mathbf{x}, \mathbf{v}_{\text{po}})$  incorporating the noise terms is given by:

$$\mathbf{0} = \mathbf{h}_{\text{po}}(\mathbf{x}, \mathbf{v}_{\text{po}}) \triangleq {}^W\mathbf{T}_I {}^I\mathbf{T}_L ({}^L\mathbf{p} + \delta_{L_{\mathbf{p}}}) - {}^W\hat{\mathbf{p}} - \delta_{w_{\hat{\mathbf{p}}}}, \quad (20)$$

where the point-to-point noise vector  $\mathbf{v}_{\text{po}}$  is defined as follows:

$$\mathbf{v}_{\text{po}} = [\delta_{L_{\mathbf{p}}}^\top, \delta_{w_{\hat{\mathbf{p}}}}^\top]^\top \in \mathbb{R}^{6 \times 1}, \quad (21)$$

where  $\delta_{w_{\hat{\mathbf{p}}}}$  is the noise term of the closest target point  ${}^W\hat{\mathbf{p}}$ .

In this work, the point-to-point residual is reformulated as an  $L_2$  norm scalar residual, which measures the Euclidean distance between corresponding points, rather than using a full vector residual [9]. This choice reduces the dimensionality of the Jacobians and covariances, leading to lower computational

overhead during state updates. It also provides a scalar residual that is consistent with the point-to-plane formulation, enabling balanced residual fusion within the hybrid-metric state update. While vector residuals may provide richer geometric constraints in structured environments, such cases are adequately addressed by the point-to-plane residuals [7] in our system.

Accordingly, the point-to-point  $L_2$  norm measurement model  $\mathbf{h}_{\text{po}}^{\text{norm}}(\mathbf{x}, \mathbf{v}_{\text{po}})$  can be defined as follows:

$$\begin{aligned} 0 &= \mathbf{h}_{\text{po}}^{\text{norm}}(\mathbf{x}, \mathbf{v}_{\text{po}}) \triangleq \|\mathbf{h}_{\text{po}}(\mathbf{x}, \mathbf{v}_{\text{po}})\| \\ &= \|\mathbf{W} \mathbf{T}_I^T \mathbf{T}_L(L \mathbf{p} + \delta_{L\mathbf{p}}) - \mathbf{W} \hat{\mathbf{p}} - \delta_{w\hat{\mathbf{p}}}\|. \end{aligned} \quad (22)$$

To compute the residual, Jacobian, and covariance, (22) is linearized at  $\hat{\mathbf{x}}^\ell$  using the chain rule and a first-order Taylor expansion, as follows:

$$0 \simeq \|\mathbf{z}_{\text{po}}^\ell\| + \frac{\mathbf{z}_{\text{po}}^{\ell \top}}{\|\mathbf{z}_{\text{po}}^\ell\|} \mathbf{H}_{\hat{\mathbf{x}}, \text{po}}^\ell \tilde{\mathbf{x}}^\ell + \frac{\mathbf{z}_{\text{po}}^{\ell \top}}{\|\mathbf{z}_{\text{po}}^\ell\|} \mathbf{H}_{\mathbf{v}, \text{po}}^\ell \mathbf{v}_{\text{po}}, \quad (23)$$

where  $\mathbf{z}_{\text{po}}^\ell (= \mathbf{h}_{\text{po}}(\hat{\mathbf{x}}^\ell, \mathbf{0}))$  is the point-to-point residual,  $\mathbf{H}_{\mathbf{v}, \text{po}}^\ell \mathbf{v}_{\text{po}} \sim \mathcal{N}(\mathbf{0}, \mathbf{R}_{\text{po}}^\ell)$  is the lumped point-to-point measurement noise,  $\mathbf{H}_{\hat{\mathbf{x}}, \text{po}}^\ell$  and  $\mathbf{H}_{\mathbf{v}, \text{po}}^\ell$  are the Jacobian matrices of  $\mathbf{h}_{\text{po}}(\hat{\mathbf{x}}^\ell \boxplus \tilde{\mathbf{x}}^\ell, \mathbf{v}_{\text{po}})$  with respect to  $\tilde{\mathbf{x}}^\ell$  and  $\mathbf{v}_{\text{po}}$ , evaluated at zero, respectively.  $\mathbf{z}_{\text{po}}^\ell$ ,  $\mathbf{H}_{\hat{\mathbf{x}}, \text{po}}^\ell$  and  $\mathbf{H}_{\mathbf{v}, \text{po}}^\ell$  are expressed as

$$\begin{aligned} \mathbf{z}_{\text{po}}^\ell &= \mathbf{W} \mathbf{T}_I^{\ell T} \mathbf{T}_L L \mathbf{p} - \mathbf{W} \hat{\mathbf{p}} \in \mathbb{R}^{3 \times 1}, \\ \mathbf{H}_{\hat{\mathbf{x}}, \text{po}}^\ell &= \left[ \mathbf{I}_3, -\mathbf{W} \mathbf{R}_I^{\ell T} \mathbf{R}_L [L \mathbf{p}]_{\times}, \mathbf{0}_{3 \times 12} \right] \in \mathbb{R}^{3 \times 18}, \\ \mathbf{H}_{\mathbf{v}, \text{po}}^\ell &= \left[ \mathbf{W} \mathbf{R}_I^{\ell T} \mathbf{R}_L, -\mathbf{I}_3 \right] \in \mathbb{R}^{3 \times 6}. \end{aligned} \quad (24)$$

Therefore, (23) can be written as follows:

$$z_{\text{po}}^{\text{norm}, \ell} + \mathbf{H}_{\hat{\mathbf{x}}, \text{po}}^{\text{norm}, \ell} \tilde{\mathbf{x}}^\ell \simeq -\frac{\mathbf{z}_{\text{po}}^{\ell \top}}{\|\mathbf{z}_{\text{po}}^\ell\|} \mathbf{H}_{\mathbf{v}, \text{po}}^\ell \mathbf{v}_{\text{po}} \sim \mathcal{N}(0, R_{\text{po}}^{\text{norm}, \ell}), \quad (25)$$

where  $z_{\text{po}}^{\text{norm}, \ell} = \|\mathbf{z}_{\text{po}}^\ell\|$ , and the Jacobian  $\mathbf{H}_{\hat{\mathbf{x}}, \text{po}}^{\text{norm}, \ell}$  and covariance  $R_{\text{po}}^{\text{norm}, \ell}$  are defined as

$$\begin{aligned} \mathbf{H}_{\hat{\mathbf{x}}, \text{po}}^{\text{norm}, \ell} &= \frac{\mathbf{z}_{\text{po}}^{\ell \top}}{\|\mathbf{z}_{\text{po}}^\ell\|} \mathbf{H}_{\hat{\mathbf{x}}, \text{po}}^\ell \in \mathbb{R}^{1 \times 18}, \\ R_{\text{po}}^{\text{norm}, \ell} &= \frac{\mathbf{z}_{\text{po}}^{\ell \top}}{\|\mathbf{z}_{\text{po}}^\ell\|} \mathbf{R}_{\text{po}}^\ell \frac{\mathbf{z}_{\text{po}}^\ell}{\|\mathbf{z}_{\text{po}}^\ell\|} \in \mathbb{R}. \end{aligned} \quad (26)$$

Here,  $\mathbf{R}_{\text{po}}^\ell$  is given by

$$\mathbf{R}_{\text{po}}^\ell = \mathbf{H}_{\mathbf{v}, \text{po}}^\ell \Sigma_{L\mathbf{p}, w\hat{\mathbf{p}}} \mathbf{H}_{\mathbf{v}, \text{po}}^{\ell \top} \in \mathbb{R}^{3 \times 3}, \quad (27)$$

where the noise covariance  $\Sigma_{L\mathbf{p}, w\hat{\mathbf{p}}}$  is defined as follows:

$$\Sigma_{L\mathbf{p}, w\hat{\mathbf{p}}} = \begin{bmatrix} \Sigma_{L\mathbf{p}} & \mathbf{0}_{3 \times 3} \\ \mathbf{0}_{3 \times 3} & \Sigma_{w\hat{\mathbf{p}}} \end{bmatrix} \in \mathbb{R}^{6 \times 6}, \quad (28)$$

where  $\Sigma_{w\hat{\mathbf{p}}}$  denotes the covariance of closest target point  $\mathbf{W} \hat{\mathbf{p}} \in \mathcal{P}$  (see Yuan *et al.* [11] for derivations).

In addition to the uncertainty-based point-to-point  $L_2$  norm covariance  $R_{\text{po}}^{\text{norm}, \ell}$ , we also account for the discretization error of point-to-point correspondences. As described in Sec. V-B, a set of past observation points  $\mathcal{P} = \{\mathbf{W} \hat{\mathbf{p}}_j\}_{j=1}^{N_{\text{stored}}}$  is stored in each root voxel of the map. While point-to-plane correspondences are matched to planes estimated from these accumulated points, point-to-point correspondences are matched

directly to one of the stored past observation points, making them more susceptible to discretization errors [12].

Accordingly, inspired by the map discretization error of Wu *et al.* [12], we model the variance term of the discretization error using quantities available from the voxel-pruned correspondence search described in Sec. V-B, as follows:

$$R_{\text{disc}} = \frac{N_{\text{accessed}} \cdot d_{\text{root}}^2}{N_{\text{eval}}}, \quad (29)$$

where  $d_{\text{root}}$  is the fixed root voxel size, and  $N_{\text{accessed}}$  and  $N_{\text{eval}}$  denote the numbers of candidate voxels accessed and points evaluated during the voxel-pruned point-to-point correspondence search for the query point  $\mathbf{W} \hat{\mathbf{p}}$ , respectively. This indicates that the point-to-point correspondence, derived from candidate voxels containing more sparsely distributed points, carries higher discretization-induced uncertainty.

The discretization variance  $R_{\text{disc}}$  is then incorporated with the uncertainty-based covariance  $R_{\text{po}}^{\text{norm}, \ell}$  to obtain the combined point-to-point covariance  $R_{\text{po}}^{\text{comb}, \ell}$  as follows:

$$R_{\text{po}}^{\text{comb}, \ell} = \lambda_{\text{po}} (R_{\text{po}}^{\text{norm}, \ell} + R_{\text{disc}}) \in \mathbb{R}, \quad (30)$$

where  $\lambda_{\text{po}}$  is an empirically chosen scaling factor introduced to balance the relative contribution of the point-to-point covariance against the point-to-plane covariance  $R_{\text{pl}}^\ell$ .

This scaling is motivated by the fact that  $R_{\text{pl}}^\ell$  is estimated from planes constructed using tens to hundreds of points [11], resulting in substantially lower uncertainty than  $R_{\text{po}}^{\text{norm}, \ell}$ , which is derived from only two points (i.e., the query and target). Without weight scaling, point-to-plane residuals tend to dominate the state update, causing point-to-point  $L_2$  norm residuals to be underweighted. For instance, in open or unstructured environments where point-to-plane correspondences are sparse, point-to-point  $L_2$  norm residuals can play a crucial role in providing geometric constraints; see Sec. VI-E. When their weights are excessively low, however, they cannot contribute effectively to the state update, leading to degraded estimation performance. Thus, by introducing the scaling factor  $\lambda_{\text{po}}$ , the proposed formulation enables balanced residual fusion, leading to more consistent state estimation across diverse environments.

This process is applied to all elements of  $\mathcal{C}_{\text{po}}$  (i.e., point-to-point correspondences), yielding the point-to-point  $L_2$  norm residuals  $z_{\text{po}}^{\text{norm}, \ell}$ , Jacobians  $\mathbf{H}_{\hat{\mathbf{x}}, \text{po}}^{\text{norm}, \ell}$ , and combined point-to-point covariances  $R_{\text{po}}^{\text{comb}, \ell}$  for each correspondence. These terms are then utilized in the hybrid-metric state update described in Sec. V-E.

### E. Hybrid-metric state update

By combining the prior distribution in (11) with the point-to-plane and point-to-point  $L_2$  norm measurement models in (17) and (25), respectively, we obtain the posterior distribution of the state  $\mathbf{x}$ . This posterior can be equivalently represented in terms of the error-state  $\tilde{\mathbf{x}}^\ell$ , whose maximum a posteriori (MAP) estimate is given by:

$$\min_{\tilde{\mathbf{x}}^\ell} \left( \|\mathbf{x} \boxminus \hat{\mathbf{x}}\|_{\hat{\mathbf{P}}}^2 + \sum_{i=1}^N \|\mathbf{z}_i^\ell + \mathbf{H}_{\hat{\mathbf{x}}, i}^\ell \tilde{\mathbf{x}}^\ell\|_{\mathbf{R}_i^\ell}^2 \right), \quad (31)$$

where  $\|\mathbf{a}\|_{\mathbf{M}}^2 \triangleq \mathbf{a}^\top \mathbf{M}^{-1} \mathbf{a}$ , and  $\sum_{i=1}^N \|z_i^\ell + \mathbf{H}_{\tilde{\mathbf{x}},i}^\ell \tilde{\mathbf{x}}^\ell\|_{\mathbf{R}_i^\ell}^2$  can be expressed as follows:

$$\begin{aligned} \sum_{i=1}^N \|z_i^\ell + \mathbf{H}_{\tilde{\mathbf{x}},i}^\ell \tilde{\mathbf{x}}^\ell\|_{\mathbf{R}_i^\ell}^2 &= \sum_{j=1}^{N_{\text{pl}}} \|z_{\text{pl},j}^\ell + \mathbf{H}_{\tilde{\mathbf{x}},\text{pl},j}^\ell \tilde{\mathbf{x}}^\ell\|_{\mathbf{R}_{\text{pl},j}^\ell}^2 \\ &\quad + \sum_{k=1}^{N_{\text{po}}} \|z_{\text{po},k}^{\text{norm},\ell} + \mathbf{H}_{\tilde{\mathbf{x}},\text{po},k}^{\text{norm},\ell} \tilde{\mathbf{x}}^\ell\|_{\mathbf{R}_{\text{po},k}^{\text{comb},\ell}}^2, \end{aligned} \quad (32)$$

where  $N_{\text{pl}}$  and  $N_{\text{po}}$  denote the number of point-to-plane and point-to-point correspondences, respectively, with  $N = N_{\text{pl}} + N_{\text{po}}$ . Furthermore, the overall residual vector  $\mathbf{z}^\ell$ , Jacobian matrix  $\mathbf{H}_{\tilde{\mathbf{x}}}^\ell$ , and covariance matrix  $\mathbf{R}^\ell$  are constructed by stacking the terms from point-to-plane and point-to-point correspondences. That is,  $z_{\text{pl}}^\ell$  and  $z_{\text{po}}^{\text{norm},\ell}$  form the residual  $\mathbf{z}^\ell$ ,  $\mathbf{H}_{\tilde{\mathbf{x}},\text{pl}}^\ell$  and  $\mathbf{H}_{\tilde{\mathbf{x}},\text{po}}^{\text{norm},\ell}$  form the Jacobian matrix  $\mathbf{H}_{\tilde{\mathbf{x}}}^\ell$ , and  $R_{\text{pl}}^\ell$  and  $R_{\text{po}}^{\text{comb},\ell}$  constitute the block-diagonal covariance matrix  $\mathbf{R}^\ell$ .

This MAP problem can be solved by error-state iterated Kalman filter [6] as follows:

$$\begin{aligned} \mathbf{K}^\ell &= (\mathbf{H}_{\tilde{\mathbf{x}}}^{\ell\top} (\mathbf{R}^\ell)^{-1} \mathbf{H}_{\tilde{\mathbf{x}}}^\ell + (\mathbf{P}^\ell)^{-1})^{-1} \mathbf{H}_{\tilde{\mathbf{x}}}^{\ell\top} (\mathbf{R}^\ell)^{-1}, \\ \tilde{\mathbf{x}}^{\ell+1} &= \tilde{\mathbf{x}}^\ell \boxplus (-\mathbf{K}^\ell \mathbf{z}^\ell - (\mathbf{I} - \mathbf{K}^\ell \mathbf{H}_{\tilde{\mathbf{x}}}^\ell) (\mathbf{J}^\ell)^{-1} (\tilde{\mathbf{x}}^\ell \boxminus \hat{\mathbf{x}})), \end{aligned} \quad (33)$$

where  $\mathbf{z}^\ell \in \mathbb{R}^{N \times 1}$ ,  $\mathbf{H}_{\tilde{\mathbf{x}}}^\ell \in \mathbb{R}^{N \times 18}$ ,  $\mathbf{R}^\ell \in \mathbb{R}^{N \times N}$ , and  $\mathbf{P}^\ell \in \mathbb{R}^{18 \times 18}$  are defined as follows:

$$\begin{aligned} \mathbf{z}^\ell &= [z_{\text{pl},1}^\ell, \dots, z_{\text{pl},N_{\text{pl}}}^\ell, z_{\text{po},1}^{\text{norm},\ell}, \dots, z_{\text{po},N_{\text{po}}}^{\text{norm},\ell}]^\top, \\ \mathbf{H}_{\tilde{\mathbf{x}}}^\ell &= [\mathbf{H}_{\tilde{\mathbf{x}},\text{pl},1}^{\ell\top}, \dots, \mathbf{H}_{\tilde{\mathbf{x}},\text{pl},N_{\text{pl}}}^{\ell\top}, \mathbf{H}_{\tilde{\mathbf{x}},\text{po},1}^{\text{norm},\ell\top}, \dots, \mathbf{H}_{\tilde{\mathbf{x}},\text{po},N_{\text{po}}}^{\text{norm},\ell\top}]^\top, \\ \mathbf{R}^\ell &= \text{diag}(R_{\text{pl},1}^\ell, \dots, R_{\text{pl},N_{\text{pl}}}^\ell, R_{\text{po},1}^{\text{comb},\ell}, \dots, R_{\text{po},N_{\text{po}}}^{\text{comb},\ell}), \\ \mathbf{P}^\ell &= (\mathbf{J}^\ell)^{-1} \hat{\mathbf{P}} (\mathbf{J}^\ell)^{-\top}, \end{aligned} \quad (34)$$

where  $\mathbf{J}^\ell$  is the partial differentiation of  $(\tilde{\mathbf{x}}^\ell \boxplus \tilde{\mathbf{x}}^\ell) \boxminus \hat{\mathbf{x}}$  with respect to  $\tilde{\mathbf{x}}^\ell$  evaluated at zero [6]. Note that computing the Kalman gain  $\mathbf{K}^\ell$  requires inverting a matrix of the state dimension instead of the measurement dimension [26].

The previous process in Sec. V repeats until convergence (i.e.,  $\|\tilde{\mathbf{x}}^{\ell+1} \boxminus \tilde{\mathbf{x}}^\ell\| < \tau_{\text{converge}}$ ). After convergence, the optimal state and covariance estimates are updated as follows:

$$\bar{\mathbf{x}} = \tilde{\mathbf{x}}^{\ell+1}, \quad \bar{\mathbf{P}} = (\mathbf{I} - \mathbf{K}^\ell \mathbf{H}_{\tilde{\mathbf{x}}}^\ell) \mathbf{P}^\ell. \quad (35)$$

With the updated state  $\bar{\mathbf{x}}$ , each LiDAR point  $L\mathbf{p}_i$  in the  $\mathcal{V}_{\text{merge},t}$ , which is obtained in Sec. IV-F, is transformed to global world frame as follows:

$${}^W \bar{\mathbf{p}}_i = {}^W \bar{\mathbf{T}}_I {}^J \mathbf{T}_L L\mathbf{p}_i; \quad i = 1, \dots, N_{\text{merge},t}, \quad (36)$$

where  $N_{\text{merge},t}$  is the number of points in  $\mathcal{V}_{\text{merge},t}$ . Then, the transformed LiDAR points are merged into the voxel map [11]. Our hybrid-metric state update is summarized in Algorithm 3.

## VI. EXPERIMENTAL EVALUATION

The main focus of this work is to develop a LIO framework that remains robust and computationally efficient across a wide range of scene scales, including indoor, outdoor, and transitional environments. We present a series of experiments to demonstrate the capabilities of our method and to support our key claims.

---

### Algorithm 3: Hybrid-metric state update in ESIKF

---

**Input** : Propagated state  $\hat{\mathbf{x}}$ ; propagated covariance  $\hat{\mathbf{P}}$ ; voxelized scan  $\mathcal{V}_t$ ; voxel map  $\mathcal{G}$ ; convergence threshold  $\tau_{\text{converge}}$ .

**Output**: Updated state  $\bar{\mathbf{x}}$ ; updated covariance  $\bar{\mathbf{P}}$ .

- 1  $\hat{\mathbf{x}}^0 \leftarrow \hat{\mathbf{x}}; \quad \ell \leftarrow -1;$
- 2 **repeat**
- 3      $\ell \leftarrow \ell + 1;$
- 4      $\mathcal{C}_{\text{pl}}, \mathcal{C}_{\text{po}} \leftarrow \text{GetCorrespondences}(\mathcal{V}_t, \mathcal{G}, \hat{\mathbf{x}}^\ell);$
- 5      $\{z_{\text{pl},j}^\ell, \mathbf{H}_{\tilde{\mathbf{x}},\text{pl},j}^\ell, R_{\text{pl},j}^\ell\}_{j=1}^{N_{\text{pl}}} \leftarrow$   
        $\text{SetPointToPlaneTerms}(\mathcal{C}_{\text{pl}}, \hat{\mathbf{x}}^\ell);$
- 6      $\{z_{\text{po},k}^{\text{norm},\ell}, \mathbf{H}_{\tilde{\mathbf{x}},\text{po},k}^{\text{norm},\ell}, R_{\text{po},k}^{\text{comb},\ell}\}_{k=1}^{N_{\text{po}}} \leftarrow$   
        $\text{SetPointToPointTerms}(\mathcal{C}_{\text{po}}, \hat{\mathbf{x}}^\ell);$
- 7     Construct overall residual  $\mathbf{z}^\ell$ , Jacobian  $\mathbf{H}_{\tilde{\mathbf{x}}}^\ell$ , and covariance  $\mathbf{R}^\ell$ ;
- 8     Compute prior covariance  $\mathbf{P}^\ell = (\mathbf{J}^\ell)^{-1} \hat{\mathbf{P}} (\mathbf{J}^\ell)^{-\top};$
- 9      $\mathbf{K}^\ell \leftarrow (\mathbf{H}_{\tilde{\mathbf{x}}}^{\ell\top} (\mathbf{R}^\ell)^{-1} \mathbf{H}_{\tilde{\mathbf{x}}}^\ell + (\mathbf{P}^\ell)^{-1})^{-1} \mathbf{H}_{\tilde{\mathbf{x}}}^{\ell\top} (\mathbf{R}^\ell)^{-1};$
- 10     $\tilde{\mathbf{x}}^{\ell+1} \leftarrow \tilde{\mathbf{x}}^\ell \boxplus (-\mathbf{K}^\ell \mathbf{z}^\ell - (\mathbf{I} - \mathbf{K}^\ell \mathbf{H}_{\tilde{\mathbf{x}}}^\ell) (\mathbf{J}^\ell)^{-1} (\tilde{\mathbf{x}}^\ell \boxminus \hat{\mathbf{x}}));$
- 11 **until**  $\|\tilde{\mathbf{x}}^{\ell+1} \boxminus \tilde{\mathbf{x}}^\ell\| < \tau_{\text{converge}};$
- 12  $\bar{\mathbf{x}} \leftarrow \tilde{\mathbf{x}}^{\ell+1}; \quad \bar{\mathbf{P}} \leftarrow (\mathbf{I} - \mathbf{K}^\ell \mathbf{H}_{\tilde{\mathbf{x}}}^\ell) \mathbf{P}^\ell;$
- 13 **return**  $\bar{\mathbf{x}}, \bar{\mathbf{P}}.$

---

### A. Experimental setup

1) *Public datasets*: To evaluate the performance of GenZ-LIO across a wide range of scene scales, we conduct experiments on nine public datasets: SubT-MRS [33], SuperLoc [31], 2021 HILTI [34], 2022 HILTI [35], GEODE [36], M3DGR [37], NTU-VIRAL [38], ENWIDE [39], and Oxford Spires [40].

The selected sequences, their scene characteristics, and the associated LiDAR sensors are described as follows. For SubT-MRS [33], we use Long Corridor (degenerate corridor), Laurel Cavern (unstructured cave), and Multi Floor (from confined stairs to open spaces), all recorded with a Velodyne VLP-16. For SuperLoc [31], we use Cave01, Cave02, and Cave04 (unstructured caves), together with Corridor02 (from corridor to open space), all under the VLP-16 setup. For 2021 HILTI [34], we use Basement04 and Drone Arena, which represent confined indoor environments and are recorded with a Livox MID-70. For 2022 HILTI [35], we use Exp10, Exp16, and Exp18, which include confined staircases and open hall segments, recorded with a Hesai PandarXT-32. For GEODE [36], we use Stairs (confined staircase), Waterways-Short, Waterways-Medium, and Waterways-Long (open waterways), as well as Offroad-02, Offroad-04, and Offroad-07 (open off-road spaces), all recorded with a VLP-16. For M3DGR [37], we use Corridor01 and Corridor02 (degenerate corridors), and GNSS-denial01 and GNSS-denial02 (structured outdoor spaces), recorded with a Livox AVIA. For NTU-VIRAL [38], we use SPMS01, SPMS02, and SPMS03, captured in high-altitude outdoor environments with agile drone motion, using an Ouster OS1-16. For ENWIDE [39], we use KatzenseeS and KatzenseeD (walking and running in unstructured outdoor scenes), and IntersectionS and IntersectionD (walking and running in structured outdoor spaces), all recorded with an Ouster OS0-128. For Oxford Spires [40], we use christ-church-01, christ-church-02, and

christ-church-05, as well as blenheim-palace-01, blenheim-palace-02, and blenheim-palace-05, which feature indoor–outdoor transitions and are recorded with a Hesai QT64.

2) *NarrowWide dataset*: To further evaluate performance under indoor–outdoor transition scenarios with more extreme variations in scene scale, we acquire a new dataset named *NarrowWide*. Although several existing datasets include indoor–outdoor transitions, they often provide only limited opportunities to evaluate repeated transitions across spaces with substantially different scales and structural characteristics. To complement these benchmarks, *NarrowWide* is intentionally acquired to contain more frequent and diverse scene transitions, including repeated movement into and out of confined structures of varying scene scales and structures, as illustrated in Fig. 1. The dataset is released together with the GenZ-LIO code to support reproducible research.

*NarrowWide* is collected using three platforms to cover a wide range of scene scales, including extremely confined spaces. A tracked robot platform (Teledyne FLIR Pack-Bot 510), equipped with a Livox MID-70 LiDAR and a VectorNav VN-100 IMU, is used to acquire the *Tracked-01* and *Tracked-02* sequences. In addition, four handheld sequences are recorded to complement the tracked sequences, covering not only portions of the same environment but also more confined spaces that are difficult for the tracked robot to access due to its size. Specifically, *Handheld-A-01* and *Handheld-A-02* are collected using a Velodyne VLP-16 LiDAR and a VectorNav VN-100 IMU, while *Handheld-B-01* and *Handheld-B-02* are collected using a Livox AVIA LiDAR with its built-in BMI088 IMU. For all platforms, a camera is mounted solely for visualization and is not utilized by the odometry pipeline.

For ground truth (GT) generation, we adopt a map-based trajectory estimation procedure, motivated by the GT system used in *Newer College* [41] dataset. Specifically, a high-resolution prior map of the environment is first constructed using a survey-grade 3D imaging laser scanner (Leica BLK360). Globally consistent 6-DoF GT trajectories are then obtained by adapting PALoc [42], which localizes each sequence against the prior map. For trajectory segments where localization becomes unstable, the estimated poses are manually refined to improve temporal consistency and overall accuracy.

3) *System configurations*: All experiments are conducted on a desktop PC equipped with an Intel i7-13700K CPU and 32 GB RAM. The default configuration of GenZ-LIO is as follows. The sliding window size is set to  $N_w = 5$ . The target number of voxelized points is bounded by  $[N_{\min}, N_{\max}] = [1,000, 4,000]$ . The exponent in the scale-to-setpoint mapping is fixed to  $p = 2$ . The scene scale threshold is set to  $\tau_m = 30.0$  m, and the scaling factors used for normalizing the tracking error and its derivative are fixed to  $\lambda_p = 0.1$  and  $\lambda_d = 0.2$ , respectively. The voxel size is constrained within  $[d_{\min}, d_{\max}] = [0.02, 1.0]$  m. The proportional and derivative gains are bounded by  $[K_{p,\min}, K_{p,\max}] = [1 \times 10^{-6}, 1 \times 10^{-4}]$  and  $[K_{d,\min}, K_{d,\max}] = [1 \times 10^{-9}, 1 \times 10^{-7}]$ , respectively. The root voxel size is fixed to  $d_{\text{root}} = 0.5$  m. For hybrid-metric residual fusion, the scaling factor is set to  $\lambda_{p_0} = 0.1$ .

## B. Benchmark experiments

The first experiment evaluates the odometry accuracy and divergence rate of the proposed method on 42 sequences from ten datasets, including the nine public datasets described above and the proposed *NarrowWide* dataset. This experiment supports our first claim that the proposed system consistently achieves competitive odometry estimation performance across indoor, outdoor, and transitional environments.

In this experiment, we compare GenZ-LIO against SOTA LIO systems, including FAST-LIO2 [6], Faster-LIO [27], AdaLIO [4], Point-LIO [17], LIO-EKF [12], DLIO [18], iG-LIO [19], and PV-LIO [43]. Notably, PV-LIO is a reimplementation of VoxelMap [11], extending it into a LIO framework [6], and serves as the baseline for GenZ-LIO.

In addition, two ablated variants are evaluated to isolate the effects of the proposed modules. The first variant incorporates the proposed scale-aware adaptive voxelization into the baseline while retaining only the point-to-plane error metric for residual computation during the state update (referred to as *Baseline w/ adap. vox.* in Table II). The second variant applies only the proposed hybrid-metric state update on the baseline, without using the scale-aware adaptive voxelization (referred to as *Baseline w/ hybrid-metric* in Table II). For all compared methods, the voxel size is set to 0.25 m for indoor scenes and 0.4 m for outdoor scenes. For indoor–outdoor transition scenarios, a voxel size of 0.25 m is used. The initial voxel size  $d_0$  of GenZ-LIO is configured based on the same criterion.

As presented in Table II, our method exhibited no divergence across all evaluated sequences, achieving the lowest total divergence rate (0.00%) among all compared approaches. In terms of total average absolute translational error (ATE), our method attained 0.75 m, which is the second-lowest value in the table. While *baseline with adaptive voxelization* reported the lowest total average ATE (0.46 m), this value was computed by excluding divergent cases, as indicated in the footnote of Table II. In contrast, our method reported its total average over the full benchmark without excluding any sequence. We next analyze how each proposed module contributes to the overall performance of GenZ-LIO in representative failure-prone scenarios.

The effect of the proposed scale-aware adaptive voxelization was most evident in sequences that included extremely confined scenes. Although the *Exp16* sequence of the 2022 HILTI [35] dataset was categorized as an indoor sequence, it contained both open hall segments and highly confined staircases, leading to abrupt variations in scene scale. In this sequence, most methods diverged in the confined staircases, where a fixed voxel size could cause the voxelized point count to drop sharply, resulting in insufficient geometric information for reliable state estimation. In contrast, *baseline with adaptive voxelization* remained stable by adjusting the voxel size to drive the voxelized point count toward a scale-informed setpoint; see Sec. VI-D. Similarly, AdaLIO [4], which also employs an adaptive voxelization strategy, avoided divergence on this sequence. Among the methods without adaptive voxelization, only Point-LIO [17] remained stable, likely due to its point-wise state update that partially com-

TABLE II. Absolute translational errors (ATE), reported as RMSE, for each sequence. Due to space limitations, dataset names are abbreviated as follows: SubT-MRS [33] (SM), SuperLoc [31] (SL), 2021 HILTI [34] (H'21), 2022 HILTI [35] (H'22), GEODE [36] (GD), M3DGR [37] (M3D), NTU-VIRAL [38] (NV), ENVIDE [39] (EW), and Oxford Spires [40] (OS). The best result is shown in **bold**. Note that “×” indicates the system totally failed, “-” denotes that the algorithm does not support the given sensor, and average values are computed excluding divergent cases.

Scale	Dataset / Sequence	FAST-LIO2 [6]	Faster-LIO [27]	AdaLIO [4]	Point-LIO [17]	LIO-EKF [12]	DLIO [18]	iG-LIO [19]	PV-LIO [43] (Baseline)	Baseline w/ adap. vox.	Baseline w/ hybrid-metric	Ours		
Indoor	SM	Long Corridor	1.77	9.76	1.74	29.10	26.52	2.29	<b>1.55</b>	2.01	1.90	1.90	1.90	
		Laurel Cavern	3.64	4.22	4.63	5.91	×	0.58	0.36	0.42	0.37	0.39	<b>0.34</b>	
	SL	Cave01	×	1.10	×	0.18	×	0.28	<b>0.12</b>	0.15	0.25	0.13	<b>0.12</b>	
		Cave02	4.49	0.81	3.98	6.57	×	0.57	0.43	0.43	0.44	<b>0.42</b>	0.44	
		Cave04	1.59	×	2.89	0.52	×	6.11	<b>0.17</b>	0.26	0.21	0.22	0.21	
	H'21	Basement 04	0.63	0.27	0.47	0.50	-	×	0.27	0.13	<b>0.05</b>	0.06	<b>0.05</b>	
		Drone Arena	0.19	<b>0.18</b>	0.23	0.20	-	×	×	0.20	0.20	0.20	<b>0.18</b>	
	H'22	Exp10	×	×	×	×	×	×	1.77	0.61	0.31	0.36	0.33	
		Exp16	×	×	0.74	0.95	×	×	×	×	<b>0.13</b>	×	0.20	
		Exp18	0.12	1.81	0.17	0.30	2.05	×	0.20	0.08	0.06	0.11	<b>0.04</b>	
	GD	Stairs	1.69	3.66	1.45	4.24	11.22	7.29	0.25	8.79	0.40	0.38	<b>0.24</b>	
	M3D	Corridor01	5.84	6.26	5.24	19.63	-	×	×	0.92	0.72	0.78	<b>0.57</b>	
		Corridor02	2.16	5.55	3.55	9.53	-	×	×	×	0.95	<b>0.70</b>	0.71	
		Divergence rate [%]	23.08	23.08	15.38	7.69	66.67	53.85	30.77	15.38	7.69	<b>0.00</b>	<b>0.00</b>	
		Average ATE [m]	2.21	3.36	2.28	6.47	13.26	2.85	0.57	1.27	0.46	0.47	<b>0.41</b>	
	Outdoor	GD	Waterways-Short	14.48	3.68	17.93	2.16	<b>0.64</b>	1.25	105.66	15.11	5.22	2.07	1.40
			Waterways-Medium	49.24	17.83	55.50	94.31	24.87	6.06	×	×	×	5.76	<b>4.07</b>
			Waterways-Long	146.70	×	143.06	94.80	14.49	<b>14.08</b>	×	×	×	24.19	14.28
Offroad-02			0.37	7.06	0.42	0.86	0.37	×	0.37	0.33	<b>0.30</b>	<b>0.30</b>	<b>0.30</b>	
Offroad-04			0.38	×	0.45	1.85	0.43	×	0.35	0.29	0.29	0.29	<b>0.28</b>	
Offroad-07			0.33	1.43	0.39	0.69	0.46	×	0.35	0.37	<b>0.28</b>	0.32	0.30	
NV		SPMS 01	2.73	3.26	1.82	0.87	0.64	0.96	3.44	2.89	<b>0.31</b>	<b>0.31</b>	<b>0.31</b>	
		SPMS 02	2.42	2.09	1.80	0.37	4.44	0.65	×	0.55	0.35	0.37	<b>0.34</b>	
		SPMS 03	1.59	5.24	1.03	0.37	0.52	0.39	×	2.31	<b>0.25</b>	<b>0.25</b>	<b>0.25</b>	
EW		Katzensee S	0.51	0.28	0.29	0.38	×	0.54	0.58	0.20	<b>0.18</b>	0.20	<b>0.18</b>	
		Katzensee D	0.66	0.48	0.46	0.38	7.44	×	0.63	<b>0.24</b>	0.25	<b>0.24</b>	<b>0.24</b>	
		Intersection S	0.27	0.28	8.79	36.08	×	0.34	23.74	0.19	<b>0.16</b>	0.17	0.17	
		Intersection D	26.89	56.50	2.53	63.28	×	6.36	8.47	0.26	<b>0.25</b>	<b>0.25</b>	0.26	
M3D		GNSS-denial 01	5.80	0.14	6.44	11.78	-	4.63	×	0.17	0.07	0.08	<b>0.05</b>	
		GNSS-denial 02	0.60	0.50	1.80	<b>0.48</b>	-	2.72	×	0.49	0.53	0.49	<b>0.48</b>	
		Divergence rate [%]	<b>0.00</b>	13.33	<b>0.00</b>	<b>0.00</b>	23.08	26.67	40.00	13.33	13.33	<b>0.00</b>	<b>0.00</b>	
		Average ATE [m]	16.86	7.60	16.18	20.58	5.43	3.45	15.95	1.80	<b>0.65</b>	2.35	1.53	
Indoor - Outdoor		SM	Multi Floor	×	2.84	0.64	1.71	13.41	3.47	<b>0.25</b>	×	0.28	0.37	0.26
	SL	Corridor02	1.89	2.88	1.98	1.74	65.59	1.39	1.48	0.73	0.77	<b>0.69</b>	<b>0.69</b>	
	OS	christ-church-01	0.79	0.71	0.79	1.04	9.81	0.25	<b>0.05</b>	0.81	0.49	0.57	0.47	
		christ-church-02	0.37	0.32	0.37	0.55	4.61	0.13	<b>0.12</b>	0.39	0.22	0.24	0.21	
		christ-church-05	0.32	0.32	0.32	0.44	2.04	0.15	<b>0.14</b>	0.30	0.23	0.27	0.24	
		blenheim-palace-01	0.13	0.16	0.15	0.19	14.54	0.32	×	0.29	<b>0.10</b>	0.15	<b>0.10</b>	
		blenheim-palace-02	0.24	×	0.24	0.44	0.94	0.33	×	0.26	<b>0.06</b>	0.08	0.07	
	blenheim-palace-05	0.37	0.32	0.37	×	3.01	0.45	0.12	0.26	0.11	0.11	<b>0.10</b>		
	NarrowWide	Tracked-01	0.23	<b>0.11</b>	0.17	1.48	-	×	0.28	3.71	0.21	0.24	0.16	
		Tracked-02	×	<b>0.11</b>	×	0.57	-	×	0.18	×	0.20	0.23	0.12	
		Handheld-A-01	×	×	0.47	0.20	×	×	2.26	×	0.22	<b>0.18</b>	0.19	
		Handheld-A-02	×	×	0.25	0.32	×	×	0.58	×	0.28	0.22	<b>0.15</b>	
		Handheld-B-01	1.45	0.32	6.61	×	-	×	×	×	0.24	0.38	<b>0.15</b>	
		Handheld-B-02	3.17	×	2.03	×	-	×	×	×	0.67	2.07	<b>0.17</b>	
		Divergence rate [%]	28.57	28.57	7.14	21.43	20.00	42.86	28.57	35.71	<b>0.00</b>	<b>0.00</b>	<b>0.00</b>	
		Average ATE [m]	0.90	0.81	1.11	0.79	14.24	0.81	0.55	0.84	0.29	0.41	<b>0.22</b>	
		Total divergence rate [%]	16.67	21.43	7.14	9.52	34.38	40.48	33.33	23.81	4.76	2.38	<b>0.00</b>	
		Total average ATE [m]	8.12	4.26	7.24	10.39	9.91	2.46	5.51	1.38	<b>0.46</b>	1.14	0.75	

\* Average values are computed excluding divergent cases.

compensated for the loss of geometric characteristics in highly confined regions.

The benefit of the proposed hybrid-metric state update was prominent in open outdoor environments with weak planar structure. In the Waterways-Short, Waterways-Medium, and Waterways-Long sequences of the GEODE [36] dataset, LiDAR returns were absent from the water surface, leading to a scarcity of reliable planar constraints along degenerate directions. In such scenarios, methods relying primarily on point-to-plane residuals often suffered from degraded accuracy or divergence, as reflected by the large errors or divergent cases. In contrast, *baseline with hybrid-metric state update* mitigated large errors induced by weak observability by leveraging point-to-point residuals to compensate for the lack of planar structure. The corresponding numerical analysis is discussed in Sec. VI-E. Consistent with this observation, LIO-EKF [12], which utilizes point-to-point residuals, also showed improved robustness in environments with limited planar structure.

The combined effect of the two proposed modules was further observed on the NarrowWide dataset, which contains extreme scene-scale variations. In the Handheld-A-01 and Handheld-A-02 sequences, the baseline method diverged due to a sharp reduction in voxelized point count in highly confined spaces, whereas the adaptive voxelization module helped preserve sufficient geometric constraints. In addition, the hybrid-metric state update improved robustness by exploiting point-to-point residuals when reliable point-to-plane constraints were unavailable in noisy or weakly structured regions. When both modules were jointly integrated, the full GenZ-LIO system consistently avoided divergence and achieved stable odometry estimation across all NarrowWide sequences, demonstrating the benefit of combining the two modules in challenging scale-variant environments.

### C. Comparison with adaptive voxelization strategies

The second experiment compares the proposed scale-aware adaptive voxelization with existing adaptive voxelization strategies on an indoor-outdoor sequence. This experiment supports our second claim that the scale-aware adaptive voxelization enables robust state estimation while efficiently regulating computational resources by accounting for varying scene scales.

For a fair comparison, all adaptive voxelization strategies [3]–[5] are evaluated within the same baseline LIO framework, PV-LIO [43], with the adaptive voxelization module being the only varying component. The evaluation is conducted on the Handheld-A-01 sequence of the NarrowWide dataset, which spans a wide range of scene scales, from extremely confined corners to open spaces.

For LOCUS 2.0 [3] and LIVOX-CAM [5], which aim to track a fixed target number of voxelized points, we set a fixed setpoint of  $N_{\text{desired}}^{\text{fixed}} = 3,000$  to retain adequate geometric information in open outdoor scenes. For AdaLIO [4], which adopts a threshold-based switching strategy, we set the coarse voxel size, fine voxel size, and point count threshold to  $d_{\text{coarse}}^{\text{fixed}} = 0.25$  m,  $d_{\text{fine}}^{\text{fixed}} = 0.05$  m, and  $\tau_N^{\text{fixed}} = 1,000$ , respectively. For the proposed method, the voxel size is adaptively

adjusted to track the setpoint  $N_{\text{desired},t}$  that varies based on the scale indicator  $\bar{m}_t$ , where the lower and upper bounds of  $N_{\text{desired},t}$  are set to  $N_{\text{min}} = 1,000$  and  $N_{\text{max}} = 3,000$ , respectively.

Performance is assessed in terms of both computational efficiency and odometry accuracy. Computational efficiency is evaluated using CPU usage and per-frame computation time, while odometry accuracy is measured by relative translational error (RTE) and ATE. CPU usage is reported as the system-wide processor utilization during runtime, expressed as a percentage, where 100% corresponds to the full utilization of a single CPU core. CPU usage measurements are obtained using a cross-platform system monitoring library [44].

As summarized in Table III, the proposed method achieved the best odometry accuracy while also exhibiting the lowest CPU usage and computation time among the compared adaptive voxelization strategies. As illustrated in Fig. 7, the baseline PV-LIO [43], which maintained a fixed voxel size of  $d_0 = 0.25$  m, suffered a substantial reduction in the number of voxelized points in a confined corner around 140 s and consequently diverged due to insufficient geometric constraints for reliable state estimation. In contrast, when adaptive voxelization strategies were applied to the baseline system, divergence was not observed in the confined regions. LOCUS 2.0 [3] generally maintained the predefined fixed target number of voxelized points, as illustrated in Fig. 7(c). Consequently, the number of voxelized points remained relatively high even in confined environments. This behavior resulted in relatively higher CPU usage and computation time than the other methods, as shown in Figs. 7(e) and (f).

Next, AdaLIO [4] switched the voxel size to a fine value when the number of voxelized points obtained with the coarse voxel size fell below the predefined threshold  $\tau_N^{\text{fixed}} = 1,000$ , as illustrated in Figs. 7(b) and (c). This switching behavior prevented the voxelized point count from becoming excessively low in confined environments. However, when the point count obtained with the coarse voxel size was close to the threshold  $\tau_N^{\text{fixed}}$ , frequent switching caused noticeable fluctuations in the voxelized point count, highlighting the need for continuous voxel size adjustment.

LIVOX-CAM [5] adopts a voxel size adjustment strategy similar to that of LOCUS 2.0, aiming to regulate the voxel size such that the number of voxelized points converges to a fixed target  $N_{\text{desired}}^{\text{fixed}}$ . Nevertheless, as shown in Fig. 7(c), the voxelized point count did not consistently remain at the predefined target of  $N_{\text{desired}}^{\text{fixed}} = 3,000$ . In open areas such as region D, the voxelized point count remained high, resulting in relatively higher CPU usage and computation time, as illustrated in Figs. 7(e) and (f). A detailed discussion of this tracking behavior of LIVOX-CAM is addressed in Sec. VI-D.

Unlike these methods, the proposed scale-aware adaptive voxelization estimates the scene scale and adjusts the voxel size to regulate the number of voxelized points toward a scale-informed setpoint. As shown in Fig. 7(c), in confined and narrow spaces such as regions B and C (also refer to Fig. 1 for better understanding), the proposed method operated with fewer voxelized points, reducing computational burden while maintaining stable odometry estimation. In open areas such

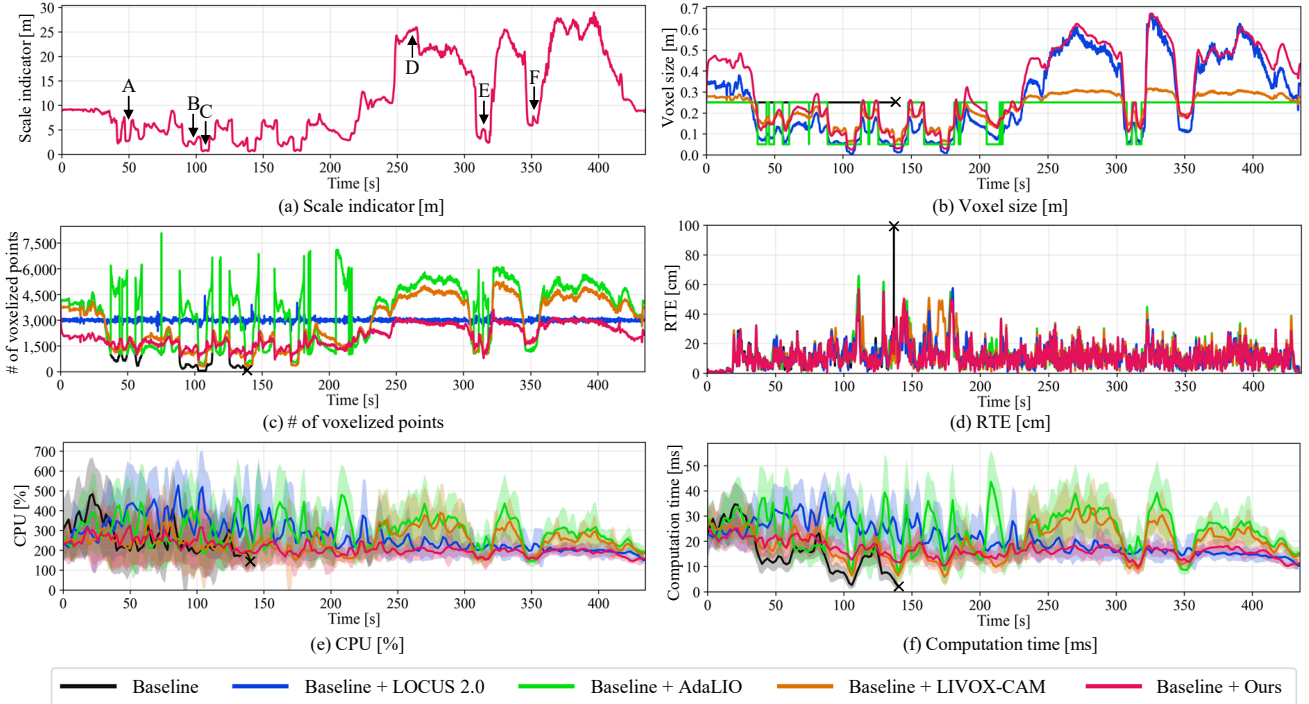


Fig. 7. Comparison of adaptive voxelization strategies [3]–[5] applied to a baseline system [43] on the Handheld-A-01 sequence of the NarrowWide dataset. (a) Temporal evolution of the proposed scale indicator  $\bar{m}_t$ . The markers A–F correspond to the regions A–F in Fig. 1, respectively. (b) Voxel sizes adjusted by each adaptive strategy. (c) Number of points in the voxelized scan obtained using the adjusted voxel size. (d) Relative translational error of the estimated poses. (e) CPU usage, visualized using a sliding-window temporal average with a shaded band indicating one standard deviation to reduce short-term fluctuations. (f) Computation time per frame, visualized using the same smoothing scheme for clarity. The baseline system diverged during the sequence and is therefore plotted only up to the divergence point, which is indicated by a  $\times$  marker. These results are further summarized in Table III.

as region D, the voxelized point count was maintained at a higher level while still being bounded by the upper limit  $N_{\max} = 3,000$ . These results show that accounting for scene scale enables the proposed method to maintain stable odometry estimation while using computational resources more efficiently across varying environments.

#### D. Ablation study on sensitivity-informed gain scheduling

The third experiment conducts an ablation study on the proposed sensitivity-informed gain scheduling to analyze its effect on tracking the desired number of voxelized points. This experiment supports our third claim that the sensitivity-informed gain scheduling improves transient response, resulting in faster convergence and reduced overshoot and oscillations during voxel size control.

The evaluation is conducted on the Exp16 sequence of the 2022 HILTI [35] dataset, which exhibits abrupt and severe scene scale variations and thus poses a challenging test case for voxel size control. To evaluate setpoint tracking performance, we employ two standard control performance indices: the integral of absolute error (IAE) and overshoot. The IAE, which measures the cumulative tracking error over the entire sequence, is defined over  $T$  discrete time steps as  $\sum_{t=1}^T |N_t - N_{\text{desired},t}| \Delta t_{\text{scan}}$ , where  $N_t$  denotes the number of points in the voxelized scan  $\mathcal{V}_t$  obtained with the updated voxel size  $d_t$ . Overshoot is defined as  $\max_{1 \leq t \leq T} \frac{N_t - N_{\text{desired},t}}{N_{\text{desired},t}}$ , which quantifies the maximum relative extent to which the response exceeds the desired setpoint. Together, these metrics capture overall tracking accuracy and transient oscillatory

TABLE III. Comparison of computational efficiency and odometry accuracy for different adaptive voxelization strategies evaluated on the Handheld-A-01 sequence of the NarrowWide dataset. CPU usage and computation time are reported using the mean and the 95th percentile (p95). RTE and ATE denote the relative and absolute translational errors, respectively, both reported as RMSE. All adaptive voxelization methods [3]–[5] are evaluated within the same baseline framework [43]. The shaded baseline row reports CPU usage and computation time only up to the divergence point and is therefore excluded from direct comparison. The symbol “ $\times$ ” indicates complete system failure, and the best performance is highlighted in **bold**. The temporal behavior of each method over the sequence is further illustrated in Fig. 7.

Method	CPU [%]		Comp. time [ms]		RTE [cm]	ATE [m]
	Mean	p95	Mean	p95	RMSE	RMSE
Baseline [43]	270.12	485.02	16.83	36.70	$\times$	$\times$
+ LOCUS 2.0 [3]	273.92	477.59	20.98	42.65	1.49	0.29
+ AdaLIO [4]	294.57	467.87	24.14	50.35	1.56	0.34
+ LIVOX-CAM [5]	245.93	372.98	19.60	34.59	1.60	0.30
+ Ours	<b>212.23</b>	<b>314.16</b>	<b>16.64</b>	<b>26.24</b>	<b>1.42</b>	<b>0.16</b>

behavior during voxel size control. Additionally, we evaluate the RMSE of the ATE to assess odometry estimation accuracy. By jointly considering IAE, overshoot, and ATE, this ablation study examines not only how effectively each method regulates voxelized point count, but also how such regulation affects downstream odometry performance.

We compare six control strategies: the *linear scaling strategy* proposed by LOCUS 2.0 [3] (Fig. 2(a)); the *volume-based scaling strategy* proposed by LIVOX-CAM [5] (Fig. 2(c)); a PD controller with fixed gains (referred to as *Fixed gains* in Table IV), where the proportional and derivative gains are set to the midpoints of their respective bounds, i.e.,  $K_{p,t} = \frac{K_{p,\min} + K_{p,\max}}{2}$  and  $K_{d,t} = \frac{K_{d,\min} + K_{d,\max}}{2}$ ; our method

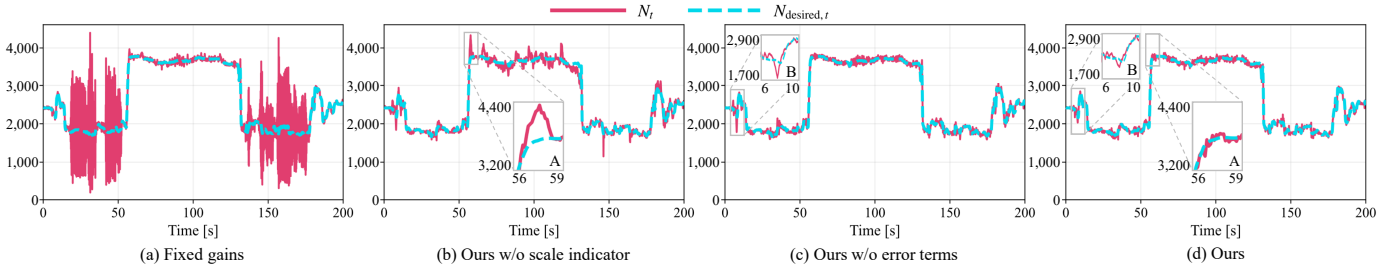


Fig. 8. Setpoint tracking performance comparison on the  $\text{Exp}_{16}$  sequence of the 2022 HILTI [35] dataset. The plots show the temporal evolution of the scale-informed setpoint  $N_{\text{desired},t}$  and the corresponding voxelized point count  $N_t$  for the following ablations: (a) PD controller with fixed gains, (b) ours without scale indicator  $\bar{m}_t$ , (c) ours without error terms  $|e_t|$  and  $|\Delta e_t|$ , and (d) ours with sensitivity-informed gain scheduling. The region A in (b) and region B in (c) correspond to the zoomed regions in (d), highlighting differences in local tracking behavior.

without the scale indicator (referred to as *Ours w/o scale indicator* in Table IV); our method without the magnitudes of the tracking error and its derivative (referred to as *Ours w/o error terms* in Table IV); and the full sensitivity-informed gain scheduling proposed in this work, as illustrated in Fig. 2(d). All methods are intentionally configured to use the same scale indicator  $\bar{m}_t$  and the same scale-to-setpoint mapping for generating  $N_{\text{desired},t}$ , and are evaluated within the same baseline odometry framework, PV-LIO [43]. That is, once  $N_{\text{desired},t}$  is determined, only the voxel size control strategy is varied, allowing the ablation to isolate the effect of different control mechanisms.

The results of all methods are summarized in Table IV. Compared with the scaling-based control strategies [3], [5], our method (i.e., sensitivity-informed gain scheduling) achieved substantially lower IAE, overshoot, and ATE, indicating more accurate and stable setpoint tracking. The particularly large IAE of the volume-based scaling strategy [5] can be attributed to its voxel size update mechanism. Specifically, volume-based scaling computes the next voxel size from a fixed reference voxel size  $d_{\text{temp}}^{\text{fixed}}$  that is not recursively updated over time. As a result, when the discrepancy between this fixed reference and the proper voxel size becomes large, the update can under- or over-adjust the voxel size, causing persistent tracking error to accumulate over the sequence.

Compared with the PD controller with fixed gains, the benefit of gain scheduling is also clear. As shown in Fig. 8(a), when the scene scale becomes small, the voxelized point count becomes highly sensitive to voxel size changes, so fixed gains can easily induce oscillatory behavior. Among the ablated variants, removing the scale indicator led to noticeable overshoot when the scene scale changed rapidly, as shown in Fig. 8(b), whereas removing the error-related terms weakened corrective action when large deviations from the setpoint occurred, as shown in Fig. 8(c). By contrast, the proposed method jointly adjusts the gains according to both the scene scale and the tracking condition, thereby reducing overshoot while improving convergence.

The observed setpoint tracking behaviors are also reflected in odometry accuracy. Methods with unstable tracking and larger oscillations tended to yield higher ATE, whereas the proposed method reduced such oscillations through more stable control and thereby achieved the lowest ATE. These results indicate that stable setpoint tracking is beneficial not only for voxel size control but also for accurate odometry estimation.

TABLE IV. Ablation study results on voxel size control strategies for tracking a scale-informed setpoint  $N_{\text{desired},t}$ , evaluated on the  $\text{Exp}_{16}$  sequence of the 2022 HILTI [35] dataset. IAE denotes the integral of absolute error. All control methods are evaluated within the same baseline odometry framework. The best performance is highlighted in **bold**.

Method	IAE [ $\times 10^3$ ] $\downarrow$	Overshoot $\downarrow$	ATE [m] $\downarrow$
Linear scaling [3]	14.03	0.24	0.21
Volume-based scaling [5]	270.71	0.87	0.34
Fixed gains	53.74	1.63	0.24
Ours w/o scale indicator	13.32	0.16	0.19
Ours w/o error terms	7.95	0.15	0.21
Ours	<b>6.04</b>	<b>0.09</b>	<b>0.13</b>

#### E. Effect of hybrid-metric state update on directionally insufficient planar constraints

The fourth experiment discusses the effect of the proposed hybrid-metric state update. This experiment supports our fourth claim that the hybrid-metric [8] state update mitigates LiDAR degeneracy caused by directionally insufficient planar constraints through the joint use of point-to-plane [7] and point-to-point [9] error metrics.

We consider two scenarios in which planar constraints become insufficient along several directions: the Waterways-Short sequence of the GEODE [36] dataset and the Handheld-B-02 sequence of the NarrowWide dataset. To numerically analyze LiDAR degeneracy, we use the condition number as a degeneracy indicator [8], [45]–[48]. We compare three configurations: the baseline system [43], which relies only on the point-to-plane error metric; the baseline with the proposed scale-aware adaptive voxelization; and the full GenZ-LIO system, which further incorporates the proposed hybrid-metric state update. Note that the corresponding odometry accuracy results are included in Table II.

As shown in Fig. 9, the full system achieved the lowest condition numbers in both scenarios, indicating the strongest mitigation of geometric degeneracy. On the Waterways-Short sequence, the baseline exhibited large condition numbers and severe drift, whereas applying only the scale-aware adaptive voxelization reduced the condition number but still left substantial degeneracy. By contrast, the full system further reduced the condition number and achieved the lowest ATE of 1.40 m. This result is consistent with the scene characteristics in Fig. 10, where the waterway environment provides weak planar constraints for the  $x$ - and  $z$ -axis translations and the pitch rotation. In this setting, the proposed hybrid-metric state update forms additional point-to-point constraints for

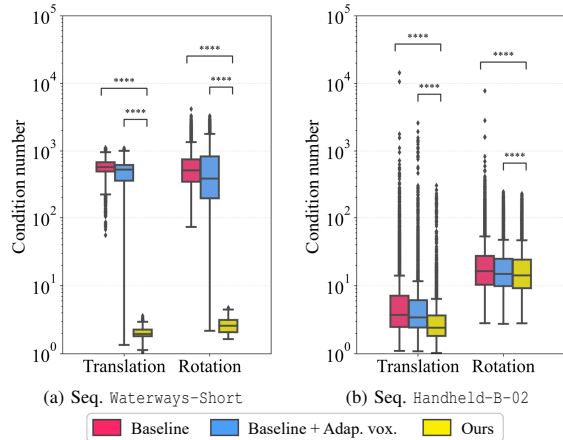


Fig. 9. Box plots of the condition number on (a) the *Waterways-Short* sequence of the *GEODE* [36] dataset and (b) the *Handheld-B-02* sequence of the *NarrowWide* dataset, evaluated by applying the proposed modules to the baseline system [43]. A lower condition number indicates improved numerical stability of the system [49]. The \*\*\*\* annotations indicate measurements with  $p$ -value  $< 10^{-4}$  after a paired  $t$ -test.

correspondences in non-planar regions, thereby strengthening observability along the degenerate directions.

A similar trend was observed on the *Handheld-B-02* sequence. Although the overall condition numbers were lower than those of *Waterways-Short*, the baseline still suffered from severe degeneracy and eventually diverged. Applying only the scale-aware adaptive voxelization improved stability and reduced the condition number, yielding an ATE of 0.67 m, whereas the full system achieved the lowest condition number and the best odometry accuracy, with an ATE of 0.17 m. These results indicate that the hybrid-metric state update is most effective when combined with scale-aware adaptive voxelization: the latter preserves a sufficient number of voxelized points, while the former improves robustness under directionally insufficient planar constraints.

#### F. Ablation study on voxel-pruned correspondence search

The fifth experiment performs an ablation study on the proposed voxel-pruned correspondence search to quantify its impact on computation time. This experiment supports our fifth claim that the voxel-pruned correspondence search algorithm substantially reduces computation time by pruning redundant traversal of neighboring voxels.

As discussed in Sec. VI-E, the hybrid-metric state update improves robustness by incorporating point-to-point constraints when planar information is insufficient. However, point-to-point correspondence search can introduce substantial computational overhead, since each candidate voxel may contain tens to hundreds of accumulated points and nearest-neighbor distance evaluations must be repeated across multiple voxels.

To examine how effectively the proposed pruning strategy alleviates this cost, we compare three correspondence search strategies on the *Offroad-04* sequence of the *GEODE* [36] dataset using two systems: *GenZ-LIO*, which jointly uses point-to-plane and point-to-point error metrics, and *LIO-EKF* [12], which relies only on the point-to-point error metric.

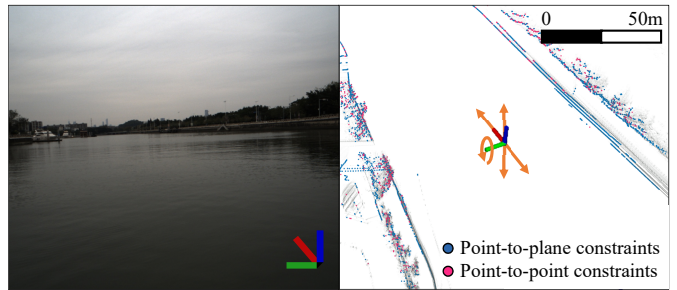


Fig. 10. Mapping result of *GenZ-LIO* on the *Waterways-Short* sequence of the *GEODE* [36] dataset. Translational and rotational directions that are weakly constrained due to insufficient geometric constraints, and are therefore susceptible to LiDAR degeneracy, are indicated by orange arrows. The visualized coordinate frame corresponds to the robot body frame, and the camera image is included solely for improved scene understanding.

The compared strategies are: 1) searching the root voxel and all 26 neighboring voxels [10], [12], 2) searching the root voxel and only its 6 surface-sharing neighboring voxels [50], and 3) the proposed voxel-pruned correspondence search. In addition to computation time, we also compare the RMSE of the ATE to examine whether reducing the search space affects odometry accuracy.

As shown in Fig. 11, the proposed voxel-pruned correspondence search achieved the lowest correspondence search time in both *GenZ-LIO* and *LIO-EKF*, while maintaining accuracy comparable to the other strategies. Searching all neighboring voxels incurred the highest computation time, whereas restricting the search to only surface-sharing neighbors reduced the cost but still left unnecessary voxel traversals. By contrast, the proposed strategy achieved the largest reduction in correspondence search time in both frameworks, which supports the effectiveness of selecting only query-adjacent neighboring voxels and pruning accesses that cannot yield a closer correspondence.

The ATEs in Fig. 11 also show that these reductions in computation time did not meaningfully degrade odometry accuracy: for *GenZ-LIO*, the ATE remained unchanged across the compared strategies, while for *LIO-EKF*, only minor variations were observed. Taken together, these results show that the proposed voxel-pruned correspondence search improves computational efficiency while preserving the quality of correspondence matching and downstream odometry estimation.

## VII. CONCLUSION

In this paper, we have presented *GenZ-LIO*, a LIO framework designed to operate robustly while maintaining computational efficiency across environments with substantially different scene scales. The proposed method introduces scale-aware adaptive voxelization, which estimates the scene scale and adjusts the voxel size via a PD controller with sensitivity-informed gain scheduling to drive the voxelized point count toward the scale-informed setpoint. In addition, the hybrid-metric state update is formulated within an ESIKF to exploit complementary geometric constraints under both structured and unstructured conditions. The voxel-pruned correspondence search further reduces redundant computations introduced by point-to-point matching.

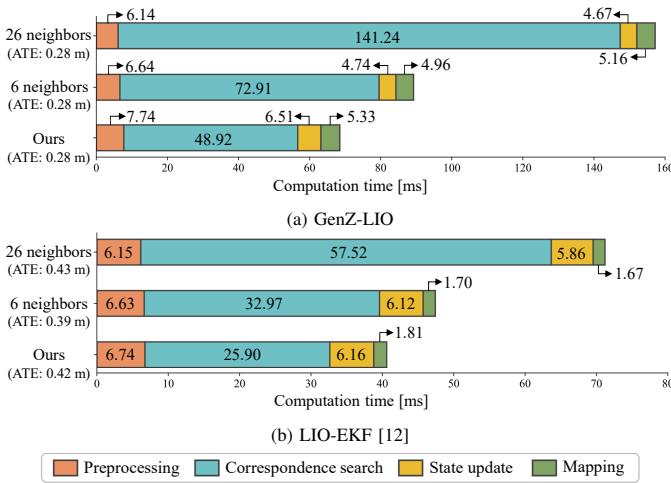


Fig. 11. Average computation time and ATE (RMSE) on the Offroad-04 sequence of the GEODE [36] dataset under different correspondence search strategies for the following LIO systems: (a) GenZ-LIO and (b) LIO-EKF [12].

Extensive evaluations on public benchmarks and the proposed NarrowWide dataset for indoor-outdoor transitions demonstrate that GenZ-LIO consistently achieves competitive accuracy without divergence. Moreover, ablation studies validate the effect of each proposed module on computational efficiency and robustness across varying scene scales. We expect that the proposed design will contribute to more reliable LiDAR-based odometry systems in real-world deployments involving frequent changes in scene scale and geometric structure. Future work will extend the proposed framework to more diverse sensor modalities, with the aim of improving generalizability across a broader range of environments and operating conditions.

## REFERENCES

- [1] D. Lee, M. Jung, W. Yang, and A. Kim, "LiDAR odometry survey: recent advancements and remaining challenges," *Intell. Serv. Robot.*, vol. 17, no. 2, pp. 95–118, 2024.
- [2] C. Cadena, L. Carlone, H. Carrillo, Y. Latif, D. Scaramuzza, J. Neira, I. Reid, and J. J. Leonard, "Past, present, and future of simultaneous localization and mapping: Toward the robust-perception age," *IEEE Trans. Robot.*, vol. 32, no. 6, pp. 1309–1332, 2016.
- [3] A. Reinke, M. Palieri, B. Morrell, Y. Chang, K. Ebadli, L. Carlone, and A.-A. Agha-Mohammadi, "LOCUS 2.0: Robust and computationally efficient LiDAR odometry for real-time 3D mapping," *IEEE Robot. Automat. Lett.*, vol. 7, no. 4, pp. 9043–9050, 2022.
- [4] H. Lim, D. Kim, B. Kim, and H. Myung, "AdaLIO: Robust adaptive LiDAR-inertial odometry in degenerate indoor environments," in *Proc. Int. Conf. Ubiquiti. Robot.*, 2023, pp. 48–53.
- [5] X. Cheng, K. Geng, Z. Liu, T. Ma, and Y. Sun, "LIVOX-CAM: Adaptive coarse-to-fine visual-assisted LiDAR odometry for solid-state LiDAR," *IEEE Robot. Automat. Lett.*, vol. 10, no. 10, pp. 10982–10989, 2025.
- [6] W. Xu, Y. Cai, D. He, J. Lin, and F. Zhang, "FAST-LIO2: Fast direct LiDAR-inertial odometry," *IEEE Trans. Robot.*, vol. 38, no. 4, pp. 2053–2073, 2022.
- [7] S. Rusinkiewicz and M. Levoy, "Efficient variants of the ICP algorithm," in *Proc. IEEE Int. Conf. 3D Digital Imaging and Modeling*, 2001, pp. 145–152.
- [8] D. Lee, H. Lim, and S. Han, "GenZ-ICP: Generalizable and degeneracy-robust LiDAR odometry using an adaptive weighting," *IEEE Robot. Automat. Lett.*, vol. 10, no. 1, pp. 152–159, 2025.
- [9] P. Besl and N. D. McKay, "A method for registration of 3-D shapes," *IEEE Trans. Pattern Anal. Mach. Intell.*, vol. 14, no. 2, pp. 239–256, 1992.
- [10] I. Vizzo, T. Guadagnino, B. Mersch, L. Wiesmann, J. Behley, and C. Stachniss, "KISS-ICP: In defense of point-to-point ICP – Simple, accurate, and robust registration if done the right way," *IEEE Robot. Automat. Lett.*, vol. 8, no. 2, pp. 1029–1036, 2023.
- [11] C. Yuan, W. Xu, X. Liu, X. Hong, and F. Zhang, "Efficient and probabilistic adaptive voxel mapping for accurate online LiDAR odometry," *IEEE Robot. Automat. Lett.*, vol. 7, no. 3, pp. 8518–8525, 2022.
- [12] Y. Wu, T. Guadagnino, L. Wiesmann, L. Klingbeil, C. Stachniss, and H. Kuhlmann, "LIO-EKF: High frequency LiDAR-inertial odometry using extended Kalman filters," in *Proc. IEEE Int. Conf. Robot. Automat.*, 2024, pp. 13741–13747.
- [13] R. Schnabel and R. Klein, "Octree-based point-cloud compression," in *Proc. Eurographics/IEEE VGTC Symp. Point-Based Graph.*, July 2006, pp. 111–121.
- [14] R. B. Rusu and S. Cousins, "3D is here: Point cloud library (PCL)," in *Proc. IEEE Int. Conf. Robot. Automat.*, 2011, pp. 1–4.
- [15] P. Dellenbach, J.-E. Deschaud, B. Jacquet, and F. Goulette, "CT-ICP: Real-time elastic LiDAR odometry with loop closure," in *Proc. IEEE Int. Conf. Robot. Automat.*, 2022, pp. 5580–5586.
- [16] K. Chen, B. T. Lopez, A.-a. Agha-mohammadi, and A. Mehta, "Direct LiDAR odometry: Fast localization with dense point clouds," *IEEE Robot. Automat. Lett.*, vol. 7, no. 2, pp. 2000–2007, 2022.
- [17] D. He, W. Xu, N. Chen, F. Kong, C. Yuan, and F. Zhang, "Point-LIO: Robust high-bandwidth light detection and ranging inertial odometry," *Advanced Intelligent Systems*, vol. 5, no. 7, p. 2200459, 2023.
- [18] K. Chen, R. Nemiroff, and B. T. Lopez, "Direct LiDAR-inertial odometry: Lightweight LIO with continuous-time motion correction," in *2023 IEEE International Conference on Robotics and Automation (ICRA)*, 2023, pp. 3983–3989.
- [19] Z. Chen, Y. Xu, S. Yuan, and L. Xie, "iG-LIO: An incremental GICP-based tightly-coupled LiDAR-inertial odometry," *IEEE Robot. Automat. Lett.*, vol. 9, no. 2, pp. 1883–1890, 2024.
- [20] Z. Zhou, M. Yang, C. Wang, and B. Wang, "ROI-cloud: A key region extraction method for LiDAR odometry and localization," in *Proc. IEEE Int. Conf. Robot. Automat.*, 2020, pp. 3312–3318.
- [21] J. Jiao, Y. Zhu, H. Ye, H. Huang, P. Yun, L. Jiang, L. Wang, and M. Liu, "Greedy-based feature selection for efficient LiDAR SLAM," in *Proc. IEEE Int. Conf. Robot. Automat.*, 5 2021, pp. 5222–5228.
- [22] W. Li, Y. Hu, Y. Han, and X. Li, "KFS-LIO: Key-feature selection for lightweight LiDAR inertial odometry," in *Proc. IEEE Int. Conf. Robot. Automat.*, 2021, pp. 5042–5048.
- [23] P. Petracek, K. Alexis, and M. Saska, "RMS: Redundancy-minimizing point cloud sampling for real-time pose estimation," *IEEE Robot. Automat. Lett.*, vol. 9, no. 6, pp. 5230–5237, 2024.
- [24] T. Tuna, J. Nubert, Y. Nava, S. Khattak, and M. Hutter, "X-ICP: Localizability-aware LiDAR registration for robust localization in extreme environments," *IEEE Trans. Robot.*, vol. 40, pp. 452–471, 2024.
- [25] T. Tuna, J. Nubert, P. Pfreundschuh, C. Cadena, S. Khattak, and M. Hutter, "Informed, constrained, aligned: A field analysis on degeneracy-aware point cloud registration in the wild," *IEEE Trans. Field Robot.*, vol. 2, pp. 485–515, 2025.
- [26] W. Xu and F. Zhang, "FAST-LIO: A fast, robust LiDAR-inertial odometry package by tightly-coupled iterated Kalman filter," *IEEE Robot. Automat. Lett.*, vol. 6, no. 2, pp. 3317–3324, 2021.
- [27] C. Bai, T. Xiao, Y. Chen, H. Wang, F. Zhang, and X. Gao, "Faster-LIO: Lightweight tightly coupled LiDAR-inertial odometry using parallel sparse incremental voxels," *IEEE Robot. Automat. Lett.*, vol. 7, no. 2, pp. 4861–4868, 2022.
- [28] A. Segal, D. Haehnel, and S. Thrun, "Generalized-ICP," in *Robot. Sci. Syst.*, vol. 2, no. 4, 2009, p. 435.
- [29] K. Koide, M. Yokozuka, S. Oishi, and A. Banno, "Voxelized GICP for fast and accurate 3D point cloud registration," in *Proc. IEEE Int. Conf. Robot. Automat.*, 2021, pp. 11054–11059.
- [30] H. Lim, B. Kim, D. Kim, E. Mason Lee, and H. Myung, "Quatro++: Robust global registration exploiting ground segmentation for loop closing in LiDAR SLAM," *Int. J. Robot. Res.*, vol. 43, no. 5, pp. 685–715, 2024.
- [31] S. Zhao, H. Zhu, Y. Gao, B. Kim, Y. Qiu, A. M. Johnson, and S. Scherer, "SuperLoc: The key to robust LiDAR-inertial localization lies in predicting alignment risks," in *Proc. IEEE Int. Conf. Robot. Automat.*, 2025, pp. 14080–14086.
- [32] C. Zheng, W. Xu, Z. Zou, T. Hua, C. Yuan, D. He, B. Zhou, Z. Liu, J. Lin, F. Zhu, Y. Ren, R. Wang, F. Meng, and F. Zhang, "FAST-LIVO2: Fast, direct LiDAR-inertial-visual odometry," *IEEE Trans. Robot.*, vol. 41, pp. 326–346, 2025.

- [33] S. Zhao, Y. Gao, T. Wu, D. Singh, R. Jiang, H. Sun, M. Sarawata, Y. Qiu, W. Whittaker, I. Higgins, Y. Du, S. Su, C. Xu, J. Keller, J. Karhade, L. Nogueira, S. Saha, J. Zhang, W. Wang, C. Wang, and S. Scherer, "SubT-MRS dataset: Pushing SLAM towards all-weather environments," in *Proc. IEEE/CVF Conf. Comput. Vis. Pattern Recognit.*, 2024, pp. 22 647–22 657.
- [34] M. Helmberger, K. Morin, B. Berner, N. Kumar, G. Cioffi, and D. Scaramuzza, "The Hilti SLAM challenge dataset," *IEEE Robot. Automat. Lett.*, vol. 7, no. 3, pp. 7518–7525, 2022.
- [35] L. Zhang, M. Helmberger, L. F. T. Fu, D. Wisth, M. Camurri, D. Scaramuzza, and M. Fallon, "Hilti-Oxford dataset: A millimeter-accurate benchmark for simultaneous localization and mapping," *IEEE Robot. Automat. Lett.*, vol. 8, no. 1, pp. 408–415, 2023.
- [36] Z. Chen, Y. Qi, D. Feng, X. Zhuang, H. Chen, X. Hu, J. Wu, K. Peng, and P. Lu, "Heterogeneous LiDAR dataset for benchmarking robust localization in diverse degenerate scenarios," *Int. J. Robot. Res.*, vol. 45, no. 1, pp. 6–22, 2026.
- [37] D. Zhang, J. Zhang, Y. Sun, T. Li, H. Yin, H. Xie, and J. Yin, "Towards robust sensor-fusion ground SLAM: A comprehensive benchmark and a resilient framework," *arXiv preprint arXiv:2507.08364*, 2025.
- [38] T.-M. Nguyen, S. Yuan, M. Cao, Y. Lyu, T. H. Nguyen, and L. Xie, "NTU VIRAL: A visual-inertial-ranging-LiDAR dataset, from an aerial vehicle viewpoint," *Int. J. Robot. Res.*, vol. 41, no. 3, pp. 270–280, 2022.
- [39] P. Pfreundschuh, H. Oleynikova, C. Cadena, R. Siegwart, and O. Andersson, "COIN-LIO: Complementary intensity-augmented LiDAR inertial odometry," in *Proc. IEEE Int. Conf. Robot. Automat.*, 2024, pp. 1730–1737.
- [40] Y. Tao, M. Á. Muñoz-Bañón, L. Zhang, J. Wang, L. F. T. Fu, and M. Fallon, "The oxford spires dataset: Benchmarking large-scale LiDAR-visual localisation, reconstruction and radiance field methods," *Int. J. Robot. Res.*, 2025, doi: 10.1177/02783649251369905.
- [41] M. Ramezani, Y. Wang, M. Camurri, D. Wisth, M. Mattamala, and M. Fallon, "The newer college dataset: Handheld LiDAR, inertial and vision with ground truth," in *Proc. IEEE/RSJ Int. Conf. Intell. Robot. Syst.*, 2020, pp. 4353–4360.
- [42] X. Hu, L. Zheng, J. Wu, R. Geng, Y. Yu, H. Wei, X. Tang, L. Wang, J. Jiao, and M. Liu, "PALoc: Advancing SLAM benchmarking with prior-assisted 6-DoF trajectory generation and uncertainty estimation," *IEEE Trans. Mechatronics*, vol. 29, no. 6, pp. 4297–4308, 2024.
- [43] "PV-LIO: A probabilistic voxelmap-based LiDAR-inertial odometry." Accessed: Dec. 23, 2025. [Online.] Available: <https://github.com/HViktorTsoi/PV-LIO>.
- [44] "Psutil." Accessed: Jan. 15, 2026. [Online.] Available: <https://psutil.readthedocs.io/en/latest/>.
- [45] J. Zhang, M. Kaess, and S. Singh, "On degeneracy of optimization-based state estimation problems," in *Proc. IEEE Int. Conf. Robot. Automat.*, 2016, pp. 809–816.
- [46] K. Ebadi, M. Palieri, S. Wood, C. Padgett, and A.-a. Aghamohammadi, "DARE-SLAM: Degeneracy-aware and resilient loop closing in perceptually-degraded environments," *Int. J. Robot. Res.*, vol. 102, no. 1, p. 2, 2021.
- [47] A. Tagliabue, J. Tordesillas, X. Cai, A. Santamaria-Navarro, J. P. How, L. Carlone, and A.-a. Agha-mohammadi, "LION: LiDAR-inertial observability-aware navigator for vision-denied environments," in *Proc. Int. Symp. Exp. Robot.*, 2021, pp. 380–390.
- [48] E. M. Lee, K. C. Marsim, and H. Myung, "LODESTAR: Degeneracy-aware LiDAR-inertial odometry with adaptive Schmidt-Kalman filter and data exploitation," *IEEE Robot. Automat. Lett.*, vol. 11, no. 1, pp. 922–929, 2025.
- [49] W. Cheney and D. Kincaid, *Numerical mathematics and computing*, CA, USA: Brooks Cole, 1998.
- [50] L. He, B. Li, and G. Chen, "PLACE-LIO: Plane-centric LiDAR-inertial odometry," *IEEE Robot. Automat. Lett.*, vol. 10, no. 6, pp. 6231–6238, 2025.